View metadata, citation and similar papers at core.ac.uk

brought to you by CORE

provided by Edinburgh Research Explorer

THE UNIVERSITY of EDINBURGH

Edinburgh Research Explorer

Gaia Early Data Release 3

Citation for published version:
Rowell, N, Davidson, M, Lindegren, L, Leeuwen, FV, Castañeda, J, Fabricius, C, Bastian, U, Hambly, NC, Hernández, J, Bombrun, A, Evans, DW, Angeli, FD, Riello, M, Busonero, D, Crowley, C, Mora, A, Lammers, U, Gracia, G, Portell, J, Biermann, M & Brown, AGA 2021, 'Gaia Early Data Release 3: Modelling and calibration of Gaia's point and line spread functions', *Astronomy and Astrophysics*, vol. 649, A11, pp. 1-22. https://doi.org/10.1051/0004-6361/202039448

Digital Object Identifier (DOI):
10.1051/0004-6361/202039448

Link:
Link to publication record in Edinburgh Research Explorer

Document Version:
Peer reviewed version

Published In:
Astronomy and Astrophysics

General rights
Copyright for the publications made accessible via the Edinburgh Research Explorer is retained by the author(s) and / or other copyright owners and it is a condition of accessing these publications that users recognise and abide by the legal requirements associated with these rights.

Take down policy
The University of Edinburgh has made every reasonable effort to ensure that Edinburgh Research Explorer content complies with UK legislation. If you believe that the public display of this file breaches copyright please contact openaccess@ed.ac.uk providing details, and we will remove access to the work immediately and investigate your claim.

OPEN ACCESS

Download date: 17. Aug. 2021

Astronomy & Astrophysics manuscript no. source
December 3, 2020
©ESO 2020

Gaia Early Data Release 3

Modelling and calibration of *Gaia*'s point and line spread functions

N. Rowell[1,⋆], M. Davidson[1], L. Lindegren[2], F. van Leeuwen[3], J. Castañeda[4], C. Fabricius[5], U. Bastian[6], N. C. Hambly[1], J. Hernández[7], A. Bombrun[8], D. W. Evans[3], F. De Angeli[3], M. Riello[3], D. Busonero[11], C. Crowley[8], A. Mora[10], U. Lammers[7], G. Gracia[96], J. Portell[5], M. Biermann[6], and A. G. A. Brown[12]

[1] Institute for Astronomy, School of Physics and Astronomy, University of Edinburgh, Royal Observatory, Blackford Hill, Edinburgh, EH9 3HJ, United Kingdom
[2] Lund Observatory, Department of Astronomy and Theoretical Physics, Lund University, Box 43, SE-22100, Lund, Sweden
[3] Institute of Astronomy, University of Cambridge, Madingley Road, Cambridge CB3 0HA, UK
[4] DAPCOM for Institut de Ciències del Cosmos (ICCUB), Universitat de Barcelona (IEEC-UB), Martí Franquès 1, E-08028 Barcelona, Spain
[5] Institut de Ciències del Cosmos (ICCUB), Universitat de Barcelona (IEEC-UB), Martí Franquès 1, E-08028 Barcelona, Spain
[6] Astronomisches Rechen-Institut, Zentrum für Astronomie der Universität Heidelberg, Mönchhofstraße 14, 69120 Heidelberg, Germany
[7] ESA, European Space Astronomy Centre, Camino Bajo del Castillo s/n, 28691 Villanueva de la Cañada, Spain
[8] HE Space Operations BV for ESA/ESAC, Camino Bajo del Castillo s/n, 28691 Villanueva de la Cañada, Spain
[9] Gaia Project Office for DPAC/ESA, Camino Bajo del Castillo s/n, 28691 Villanueva de la Cañada, Spain
[10] Aurora Technology for ESA/ESAC, Camino Bajo del Castillo s/n, 28691 Villanueva de la Cañada, Spain
[11] Istituto Nazionale di Astrofisica, Osservatorio Astrofisico di Torino, Via Osservatorio 20, Pino Torinese, Torino, 10025, Italy
[12] Leiden Observatory, Leiden University, Niels Bohrweg 2, 2333 CA Leiden, The Netherlands

ABSTRACT

Context The unprecedented astrometric precision of the *Gaia* mission relies on accurate estimates of the locations of sources in the *Gaia* data stream. This is ultimately performed by point spread function (PSF) fitting, which in turn requires an accurate reconstruction of the PSF, including calibrations of all the major dependences. These include a strong colour dependence due to *Gaia*'s broad *G* band and a strong time dependence due to the evolving contamination levels and instrument focus. Accurate PSF reconstruction is also important for photometry. *Gaia* Early Data Release 3 (EDR3) will, for the first time, use a PSF calibration that models several of the strongest dependences, leading to signficantly reduced systematic errors.
Aims We describe the PSF model and calibration pipeline implemented for *Gaia* EDR3, including an analysis of the calibration results over the 34 months of data. We include a discussion of the limitations of the current pipeline and directions for future releases. This will be of use both to users of *Gaia* data and as a reference for other precision astrometry missions.
Methods We develop models of the 1D line spread function (LSF) and 2D PSF profiles based on a linear combination of basis components. These are designed for flexibility and performance, as well as to meet several mathematical criteria such as normalisation. We fit the models to selected primary sources in independent time ranges, using simple parameterisations for the colour and other dependences. Variation in time is smoothed by merging the independent calibrations in a square root information filter, with resets at certain mission events that induce a discontinuous change in the PSF.
Results The PSF calibration shows strong time and colour dependences that accurately reproduce the varying state of the *Gaia* astrometric instrument. Analysis of the residuals reveals both the performance and the limitations of the current models and calibration pipeline, and indicates the directions for future development.
Conclusions The PSF modelling and calibration carried out for *Gaia* EDR3 represents a major step forwards in the data processing and will lead to reduced systematic errors in the core mission data products. Further significant improvements are expected in the future data releases.

Key words. instrumentation: detectors – methods: data analysis – space vehicles: instruments

1. Introduction

Gaia Early Data Release 3 (EDR3), the third release of data from the European Space Agency mission *Gaia* (Gaia Collaboration et al. 2016), contains results based on data collected during the first 34 months of the nominal mission (Gaia Collaboration et al. 2020). The principles of the *Gaia* cyclic data processing are such that each successive release is based on a complete reprocessing of the mission data collected up to the chosen cut-off point. This allows the released data to benefit from substantial improvements to various core charge-coupled device (CCD) calibration and instrument models made during the mission as the understanding of the payload develops. This is crucial in beating down systematic errors present in earlier data releases and leads to improvements in the astrometric and photometric data that are better than expected based purely on the increased quantity of raw observations. Of the core CCD calibrations—including,

⋆ Corresponding author: N. Rowell
e-mail: nr@roe.ac.uk

for example, the bias prescan and non-uniformity (Hambly et al. 2018), straylight and CCD health—the calibration and modelling of the point and line spread functions (PSF and LSF) is perhaps the most vital in terms of improving both the accuracy and precision of single-observation measurements of the location and G band flux of sources in the *Gaia* data stream, which are the quantities used to drive the astrometric and photometric (G band) solutions. We note that the LSF simply refers to the 1D image of a point source obtained by marginalising a 2D image over one dimension, which is how the majority of *Gaia* observations are made. The PSF and LSF are modelled and calibrated independently. Throughout this paper we use the acronym PLSF when referring to both the point and line spread functions.

The central goal of the PLSF calibration is to produce a model of a given stellar observation that can be used to estimate, via a separate process of image parameter determination (IPD; see section 4.7), the instrumental flux and location of the source in the *Gaia* data stream. The detailed shape of the PLSF varies significantly with time, colour, and position in the focal plane and has numerous additional dependences of varying significance, some of which are unique to *Gaia*. The accurate calibration of these effects in the PLSF is vital for the elimination of systematic errors in both the astrometry and photometry. In principle, the biases introduced by these effects can be reduced either in a statistical way during the astrometric and photometric calibration, where they manifest as structure in the residuals to the calibration, or in a direct way by absorbing them into the PLSF calibration. While the former approach was used in *Gaia* Data Release 2 (DR2) (see e.g. Lindegren et al. 2018, section 3.3), the ultimate goal is to pursue the latter approach, and EDR3 represents the first major step in achieving this. This approach enables a clear demarcation of the roles of the PLSF calibration and the astrometric and photometric calibrations, it provides the best PLSF model for use in more sophisticated image analyses, for example of extended objects or close binaries, and it allows the proper handling of less common types of observation, such as those that use non-nominal instrument configurations, for which the statistical approach does not correctly remove the biases.

In this paper we present the modelling and calibration of *Gaia*'s PSF and LSF carried out in support of EDR3. We note that these results also apply to the full DR3, as the calibrations will not be updated and the astrometry and (integrated) photometry included in EDR3 (and which make use of the PLSF calibrations) will not be recomputed. The PLSF models presented here are not the only ones used in the *Gaia* data processing. An independent model is implemented within the real-time processing systems devoted to internal scientific validation of the astrometric processing chain (see Gaia Collaboration 2020, Section 3.5.2). The PLSF models presented in this paper have been adopted in the cyclic data processing for use in production of the data releases.

2. Description of the instrument and observations

In this section we briefly review the main properties of the *Gaia* optical system, CCDs and observations that are relevant to the PLSF modelling and calibration. A more detailed description can be found in section 2 of Fabricius et al. (2016), to which the reader is referred for further information.

2.1. The optical system and focal plane instruments

The *Gaia* instruments consist of two telescopes separated by a wide 'basic angle' of 106.5° that form images on a single shared focal plane array of 106 CCDs. The CCDs are arranged into seven rows containing 13–17 columns or 'strips'; the CCDs in each row are divided among several instruments that are used to perform measurements for scientific or diagnostic purposes. In this paper we are concerned with modelling the LSF and PSF of two of the instruments, the Sky Mapper (SM) and the Astrometric Field (AF), which both observe unfiltered and undispersed light in the *Gaia* G band. The SM and AF consist of 14 and 62 CCDs respectively. The arrangement of these CCDs in the focal plane and their designation is depicted in Figure 1; the CCDs are oriented such that the readout direction is to the right. The satellite rotates about an axis perpendicular to the plane of the telescope axes, with a rotation period of ~6 hours. Stellar images drift across the focal plane from left to right in Figure 1 over a period of around a minute. The directions in the focal plane parallel and perpendicular to the stellar motion are referred to as the along-scan (AL) and across-scan (AC) directions respectively. The CCDs are operated in time-delayed integration (TDI) mode, where charge is transferred slowly at a rate that matches the stellar motion, thus allowing the charge to accumulate during readout. The TDI period, corresponding to the time taken for the charge to be transferred by one pixel in the AL direction, is 0.9828 milliseconds. The onboard mission timeline (OBMT) is used to define the timing of events on the satellite; for convenience, in this paper we express OBMT in units of 6 hours, or one revolution (rev), which corresponds (approximately) to the satellite rotation period[1]. The OBMT range covered by the EDR3 input data corresponds to 1078–5230 revs, or ~34 months.

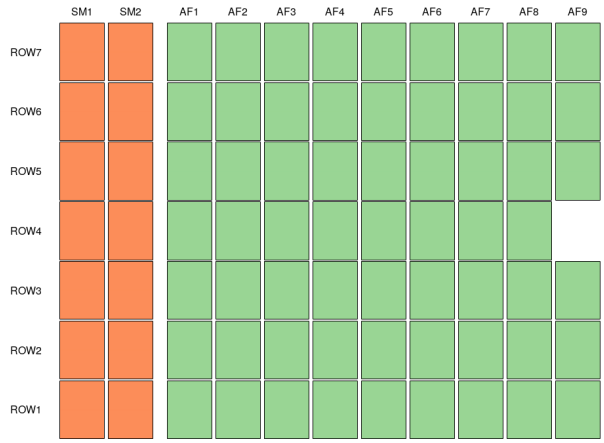

Fig. 1: Schematic of the 14 sky mapper (orange) and 62 astrometric field (green) CCDs and their arrangement in the focal plane. In this diagram, stars enter the focal plane from the left and drift slowly to the right over around a minute.

2.2. Observations of stars

The two telescopes are referred to as field of view 1 (FOV1) and 2 (FOV2). Each strip of SM CCDs sees the light from only one of the two FOVs (FOV1 for SM1 and FOV2 for SM2), then the two FOVs are superimposed on the AF strips. Each source that transits the focal plane thus has either nine (ROW4) or ten

[1] A tool for transformation between OBMT and other time systems is available at `https://gaia.esac.esa.int/decoder/obmtDecoder.jsp`; see also Equation 1 in Lindegren et al. (2018).

(ROW1–3,5–7) G band observations. The SM and AF1 CCDs are used in real-time to autonomously detect the presence of stars and other astronomical objects, estimate their magnitude and to predict their motion over the focal plane. This enables the use of windowing to sample the data and downlink only small sections surrounding each detected source. This optimises the available telemetry budget, as well as reducing the readout noise, at the expense of introducing some complications in the processing. In addition, for the great majority of windows on-chip binning is used to marginalise the AC dimension so that only a 1D profile in the AL direction is observed. This is consistent with the astrometric observing principles of *Gaia* (and indeed of Hipparcos), for which an accurate location in the AL direction is far more important. Each observation is assigned a window with a particular geometry according to its estimated magnitude and the CCD strip. The windowing is of fundamental importance to the PLSF calibration and the specification of the windows by magnitude and strip is shown in Table 1. The different window geometries split the data naturally into subsets that are labelled by window class (WC); in SM there are two window classes labelled WC0 and WC1, whereas in AF there are three window classes: WC0, WC1, and WC2. The pixel scale is such that a window of 18×12 pixels has an angular size of roughly $1''.1 \times 2''.1$ AL×AC. The combination of 2D and 1D windows necessitates the calibration of both the PSF, used to model the 2D observations, and the LSF, used to model the 1D observations.

The ~4.42 seconds that it takes a stellar image to cross an individual CCD places an upper limit on the integration time available for each source. For such an observation, the charge is accumulated over the entire AL range of the CCD. In order to expand the dynamic range of *Gaia*, bright stars that are expected to saturate the detector can be observed for a shorter integration time by the activation of special structures in the CCDs known as TDI gates. These are positioned at a range of AL locations along the readout direction and can be used to temporarily hold back the charge transfer, thus resetting the charge accumulation and reducing the integration time. The gate assignment and activation is done autonomously in real time based on the onboard estimated magnitude from the SM observation. There are eight gates routinely in use, referred to as gates 4, 7, 8, 9, 10, 11, 12, and 0 (see Gaia Collaboration et al. 2016, figure 5). The gating strategy maximises charge collection and minimises saturation for bright stars spanning three orders of magnitude in brightness. The exposure time varies from 0.016 seconds for gate 4 up to 4.42 seconds when no gate is applied (gate 0). For gates 7 to 11, the exposure time is approximately doubled for each transition. Observations taken with each gate effectively sample a different AL range of the CCD and are therefore expected to have a different PLSF, due to spatial variations within the detector area. This further splits the data into subsets that are labelled by TDI gate. Only sources with $G \lesssim 12.5$ are bright enough for TDI gates to be activated. These correspond to the WC0 observations. We note that in SM, a single gate (12) is permanently activated and no dynamic gate assignment is performed.

The CCDs also contain circuitry that enables the injection of charge into the first line of pixels (at the left side of the devices depicted in Figure 1), which then transfers through the detector at the normal rate. Periodic short bursts of injected charge are used to both mitigate and calibrate the effects of radiation-induced charge transfer inefficiency (CTI) in the image section of the CCD (Crowley et al. 2016).

2.3. Specification of independent calibration units

The SM and AF observations made by *Gaia* split naturally into different subsets over which the PLSF is calibrated independently. Each distinct combination of field of view, CCD, TDI gate and window class corresponds to one independent calibration unit. There are 248 calibration units that correspond to 1D observations for which the LSF is calibrated; these cover the 62 AF CCDs, two window classes (WC1 and WC2) and the two fields of view. In contrast, there are 1020 calibration units that correspond to 2D observations for which the PSF is calibrated. These cover the 62 AF CCDs, one window class (WC0), eight TDI gates (4, 7–12, 0) and two fields of view, plus an additional 28 calibration units corresponding to the 14 SM CCDs and two window classes (WC0 and WC1). This leads to a total of 1268 calibration units for the PLSF calibration.

3. Description of the PLSF models

The task of modelling the PSF for a telescope or image is a classic problem in astronomy and one for which various standard software packages already exist (e.g. DAOPHOT (Stetson 1987), PSFEx (Bertin 2011)). However, the extreme requirements for Gaia centroiding accuracy, the unusual PSF dependences and the highly windowed, undersampled and marginalised data motivate the development of a dedicated PLSF model and calibration pipeline tailored to the unique needs of *Gaia*.

3.1. Basics

An important point to note is that the true intrinsic or instrumental PSF, which is the 2D distribution of flux in the focal plane, is never directly observed. Instead, what is observed and calibrated is the 'effective' PSF (Anderson & King 2000) which accounts for the pixelated nature of the image, as well as a few other sources of smearing such as charge diffusion and differences between the image motion and charge transfer rate during TDI operation. As such, the PLSF models used to calibrate the effective PSF must satisfy a number of mathematical requirements. They must be continuous in value and in the first derivative. They must also have a shift invariant sum, that is to say, if either model is sampled over all space at a set of points one pixel apart, the sum must be invariant to the sub-pixel location at which the samples are drawn. This expresses the physical constraint that the total number of photoelectrons received from a source is independent of the sub-pixel location of the source, which is a good approximation for back-illuminated CCDs with high fill-factors. Enforcing this constraint in the PLSF models avoids introducing small photometric biases as a function of the sub-pixel position. One complication is that *Gaia* observes only a finite region of the PLSF due to the use of windowing, and this contains only a fraction of the total flux (the 'enclosed energy fraction', EEF). Over such a region, the shift invariant sum property does not strictly hold. The PLSF models cannot account for the EEF, and instead this effect is corrected in the photometric calibration.

The PLSF models must also be normalised, over one dimension in the case of the LSF and over two dimensions in the case of the PSF. A subtle issue that arises here is that due to the finite window extent in the AC direction the LSF model will underestimate the flux of a star relative to the PSF because the LSF model fails to account for the flux falling outside of the window in the AC direction. This AC flux loss is instead accounted for in the photometric calibration (Riello et al. 2020). Another

Table 1: Specification of the downlinked window geometry by onboard estimated G magnitude and CCD strip. In each case the window class (WC) is given followed by the number of samples in the AL and AC directions, the number of pixels in the AL and AC directions that have been binned to produce each sample (in brackets), and whether the resulting observation corresponds to the LSF or PSF. The solid black lines indicate the geometry of each sample and their arrangement to form the window; the faint dashed lines indicate the pixels that have been binned to produce each sample. A combination of on-chip and numerical (software) binning is applied to optimise onboard performance and telemetry budget.

Strip	G<13	13<G<16	16<G
SM	WC0: 40×6 (2×2) PSF 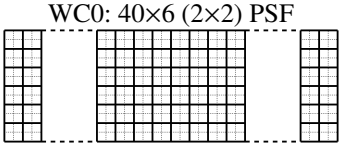	WC1: 20×3 (4×4) PSF 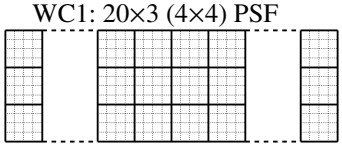	
AF1	WC0: 18×6 (1×2) PSF 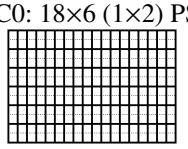	WC1: 12×1 (1×12) LSF 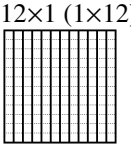	WC2: 6×1 (1×12) LSF 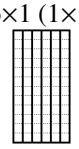
AF2–9	WC0: 18×12 (1×1) PSF 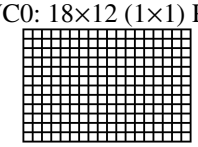	WC1: 18×1 (1×12) LSF 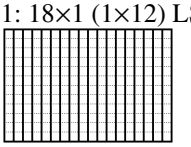	WC2: 12×1 (1×12) LSF 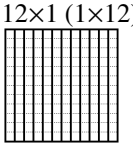

physical constraint is that the true PSF is positive everywhere, however this is not enforced and as such the calibrated model, fitted to noisy observations, can be negative in places. Similar to negative parallaxes, this does not necessarily indicate a problem and simply indicates that the true PSF value is likely to be small.

3.2. Formulation of the 1D LSF model

The model for the LSF has not changed significantly since DR2 (although the calibration has–see later), and is described extensively in the associated documentation (Hobbs et al. 2018, section 2.3.2) and in several technical notes, in particular Lindegren (2003, 2009, 2010a,b).

To recap, the LSF $L(u)$ is constructed as the linear combination of a mean profile H_0 and a weighted sum of N basis components H_n, where

$$L(u) = H_0(u - u_0) + \sum_{n=1}^{N} h_n H_n(u - u_0)\,. \tag{1}$$

The AL coordinate u has units[2] of pixels. The notation used here is slightly adapted relative to Equation 10 of Lindegren (2010a), in order to allow greater clarity when presenting both LSF and PSF models. In particular, the parameter correponding to a shift of origin is denoted u_0 rather than h_0. In EDR3 this is not considered a free parameter and is set to zero; it will be omitted in the following equations (though see section 6.7.2 for further discussion). The only free parameters of the model that need to be calibrated are the weights h_n, which are themselves multidimensional spline functions of the source colour and other parameters. The main task of the LSF calibration is thus to solve for the parameters of these multidimensional splines, which is explained further in section 3.4. The functions H in Equation 1 are represented using an 'S-spline' in the LSF core with a smooth transition to a Lorentzian profile in the wings (see Hobbs et al. 2018, section 2.3.2.1), a formulation chosen specifically to meet the shift invariant sum requirement. The particular forms of H are derived from simulations of the optical system carried out before launch, and described in Lindegren (2009). Briefly, many random realisations of the *Gaia* wavefront error map were used to generate a large set of monochromatic PSFs of various wavelengths, assuming a Fraunhofer diffraction model of *Gaia*'s optical system and applying a modulation transfer function to model the smearing effect of TDI mode, pixel binning and charge diffusion. The monochromatic PSFs were blended to produce a large set of physically plausible polychromatic PSFs for different stellar spectral energy distributions, then marginalised to obtain the AL LSFs. This set was doubled in size by including the reversed LSFs obtained by reflecting in the AL direction. A principal components analysis (PCA) was applied to these to determine the mean LSF and the basis components, resulting in a set of orthogonal functions that can be used to model the LSF and for which the truncated set gives the lowest possible RMS reconstruction error among all linear models. We note that the inclusion of the reflected LSFs has the effect of imposing odd or even symmetry on the mean LSF and the bases obtained by PCA[3], as is evident in Figure 2. These were then post-processed as described in Lindegren (2010a) to ensure that the mean is normalised such that the integral is unity and the basis components are normalised such that their integrals are zero. This guarantees that the full model is normalised to unity regardless of the basis component weights h_n. The resulting discretely sampled functions were then fitted with the S-spline model described above to obtain the final functions used in the data processing. The mean LSF and the first three basis components are shown in Figure 2. There are some points to note regarding this procedure. First, the generation of the basis components via random

[2] Also sometimes expressed in *Gaia* documentation in the equivalent unit of TDI periods. An important point is that due to the use of TDI mode, there is no correspondence between the AL coordinate and an absolute location on the detector; rather, the AL coordinate measures only displacements in the AL direction.

[3] This does not imply that the calibrated LSF formed by a weighted sum of the bases has any such symmetry—indeed, the calibrated LSF is quite asymmetric, as can be seen in Figure 11.

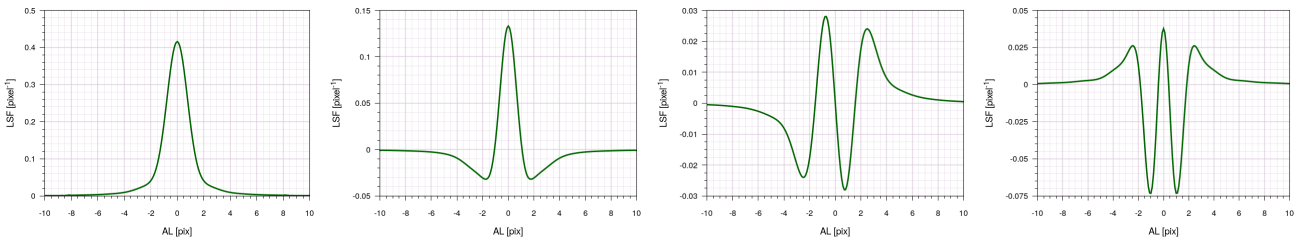

Fig. 2: Mean LSF H_0 (left) and the first three basis components H_1–H_3, used to model the LSF for both telescopes. These are obtained from simulations, with the odd or even symmetry arising from the inclusion of reflected wavefront error maps (see text).

realisations of the wavefront error map means they are in principle capable of modelling the LSF of a range of instruments according to the configuration space spanned by the wavefront error maps. The number of basis components required to reach a particular RMS reconstruction error could therefore be reduced by tailoring the bases to the in-flight *Gaia* instrument via a suitable reduction procedure (e.g. Lindegren 2010c), however this was not found to offer a significant advantage and was not done for EDR3. Second, efforts were made to determine an appropriate set of basis components directly from the data, however due to the presence of noise and the undersampled nature of the observations the resulting basis components had larger PLSF reconstruction errors than those derived from simulations. Third, it is important that all significant instrumental effects are included in the optical model, as any missing component will result in bases that cannot fully reproduce the real observations. This is expanded on in section 6.7.4. Finally, the normalisation procedure applied to the initial basis components has the side effect of introducing slight non-orthogonality. This effect is minor and was found to not compromise the numerical stability of the calibration pipeline.

3.3. Formulation of the 2D PSF model

Before describing the PSF model implemented for EDR3, some historical context is useful. The original PSF model implemented for *Gaia*, referred to in the documentation as the 'AL×AC' model, composed the 2D PSF (denoted $P(u, v)$) as the outer product of two 1D LSF models that were calibrated to the AL and AC marginal profiles:

$$\begin{aligned} P(u,v) &= L(u) \times L(v) \\ &= \left(\sum_{n=0}^{N} h_n H_n(u)\right) \times \left(\sum_{m=0}^{N} g_m H_m(v)\right) \\ &= H_0(u)H_0(v) + \sum_{n+m>0}^{\substack{n=N \\ m=N}} h_n g_m H_n(u) H_m(v)\,. \end{aligned} \tag{2}$$

where v denotes positions in the AC direction, and the factors g_m are the basis component amplitudes for the AC LSF. We note that for brevity the sum has been expanded to include the mean components, so that $h_0 = g_0 = 1$, and the same 1D functions H are used to model both the AL and AC LSFs. This was assumed to be a reasonable model for *Gaia*, given that the PSF formed by Fraunhofer diffraction of a rectangular pupil can be factored into the product of 1D functions in each dimension. Unfortunately, this fails to take into consideration the wavefront errors, which introduce significant asymmetric features that cannot be represented within this model (see Hobbs et al. 2018, figs 2.1 and 2.2). While this AL×AC model was used in the production of DR1 and DR2, it was clear that a new formulation was required for EDR3.

3.3.1. The pseudo-shapelets model

The PSF model initially developed for EDR3 was based on the shapelets idea described in Refregier (2003), where the PSF is composed as the weighted sum of 2D basis components (the shapelets) that are generated as the outer products of orthogonal 1D functions of varying order. In the original paper these were Hermite polynomials, but for application to the Gaia observations the 1D functions are the same ones used to model the LSF. The resulting PSF model is referred to as pseudo-shapelets, in light of the fact that the 1D functions are different. The full pseudo-shapelets PSF model is then

$$P(u,v) = H_0(u)H_0(v) + \sum_{n+m>0}^{\substack{n=N \\ m=N}} h_{nm} H_n(u) H_m(v)\,. \tag{3}$$

This is similar to the AL×AC model (Equation 2), with the generalisation $h_n h_m \rightarrow h_{nm}$ that allows much greater freedom in the model to reproduce asymmetric features. A selection of the low order pseudo-shapelets basis components, formed from the outer products $H_n H_m$, are presented in Figure 3.

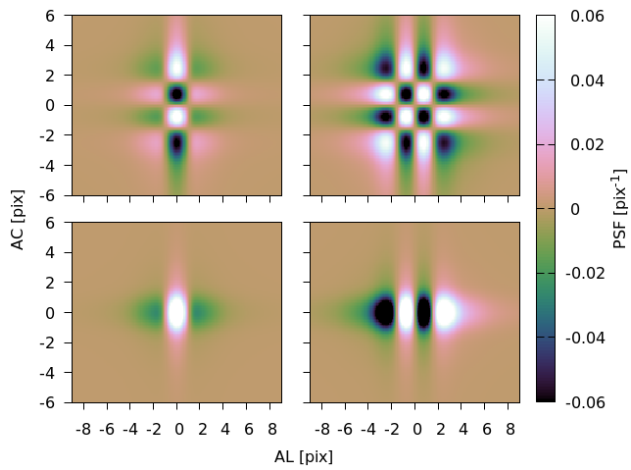

Fig. 3: Selection of low order pseudo-shapelets basis components, formed from outer products of the 1D functions as follows: $H_1(u)H_0(v)$ (bottom left), $H_2(u)H_0(v)$ (bottom right), $H_1(u)H_2(v)$ (top left), and $H_2(u)H_2(v)$ (top right). Each pseudo-shapelet has been normalised by a different amount in order to better display the structure. Throughout this paper we make use of the cubehelix colour scheme introduced in Green (2011).

While this model achieves good reconstruction of the PSF, it has the major drawback that a very large number of basis components are required. For 20 1D basis components H_n plus the mean H_0, there are 440 2D bases and an equivalent number of weights h_{nm}, which becomes a major computational challenge when scaled up to the demands of the *Gaia* data processing, from the point of view of both calibration of the model and sampling it to fit observations. In addition, many of the 2D basis components have very low importance, and there is no way to rigorously rank them to form a truncated set. Investigation of the principal components present in the real *Gaia* PSF revealed two important features. First, the observed principal components have significant asymmetric structure that cannot be well modelled by any individual pseudo-shapelet. Second, the dimensionality of the real PSF is significantly lower than 440. These observations motivated the development of the compound shapelets model that is described in the next section.

3.3.2. The compound shapelets model

The compound shapelets model is based on the pseudo-shapelets model, but rather than calibrating all the 1D×1D pseudo-shapelets individually, we instead calibrate fixed linear combinations of them that are constructed to model the principal components of the observed *Gaia* PSF. Each fixed linear combination of pseudo-shapelets provides one full 2D basis component that is referred to as a compound shapelet. The compound shapelets are computed by first calibrating the pseudo-shapelets model over a large set of *Gaia* observations that span the whole focal plane and a wide range of mission time, in order to sample a wide range of instrument states. The resulting calibrations are then post-processed using the algorithm described in Lindegren (2010c). This algorithm computes linear combinations of the input basis components (the pseudo-shapelets) resulting in a transformed set for which the information is compressed into the leading orders. This provides a minimal set of 2D bases referred to as the compound shapelets G. In terms of these, the full PSF model is

$$P(u,v) = G_0(u,v) + \sum_{m=1}^{M} g_m G_m(u,v)\,, \tag{4}$$

where

$$G_0(u,v) = H_0(u)H_0(v) + \sum_{k+l>0}^{\substack{k=N\\l=N}} \beta^0_{kl} H_k(u) H_l(v)$$

and

$$G_m(u,v) = \sum_{k+l>0}^{\substack{k=N\\l=N}} \beta^m_{kl} H_k(u) H_l(v)\,.$$

The (constant) matrix β defines the construction of the compound shapelets from the pseudo-shapelets. The only free parameters now are the weights g_m applied to the compound shapelets; for EDR3 30 basis components were used. Independent sets were generated for FOV1 and FOV2; the mean and first three bases for both FOVs are depicted in Figure 4.

3.4. Modelling of the major PLSF dependences

The observed PLSF exhibits significant variation with source colour, position in the focal plane and certain other observation parameters that must be incorporated into the model. There is also large variation in time due to the evolving instrument state. As described in section 3.4.5 we handle the time dependence in a different manner to the rest of the PLSF dependences, and it will be omitted in the following description.

All of the major PLSF dependences are ultimately modelled empirically by appropriate weighting of the PLSF basis components. The weight factors h_n and g_m are represented by multidimensional spline functions of the observation parameters, each of which is chosen to adequately parameterise the corresponding dependence. The particular spline implementation used is that described in van Leeuwen (2007, appendix B), extended to multiple dimensions according to the number of observation parameters included in the model. The set of observation parameters chosen and the spline configuration for each dimension define the configuration of the PLSF model, with the parameters of the model that need to be calibrated being the coefficients of the spline functions. For EDR3 we selected the following observation parameters for inclusion in the PLSF model. These were chosen to represent the largest dependences present. We note that source flux is not included in the parameterisation of the PLSF for EDR3; this is discussed in section 6.7.3.

3.4.1. Source colour

Because of *Gaia*'s broad G band combined with wavelength-dependent diffraction within the optical system, the PLSF profiles of stars of different spectral type show large variation. The source colour is parameterised by the 'effective wavenumber', denoted $\nu_{\rm eff}$, which is calculated as the photon-weighted inverse wavelength. $\nu_{\rm eff}$ was identified as a suitable parameterisation of the source colour as the chromatic shifts in the PLSF centroid are expected to be linear in $\nu_{\rm eff}$ (de Bruijne et al. 2006; Busonero et al. 2006). The value of $\nu_{\rm eff}$ for each source is calculated from the BP and RP spectra as part of the photometric processing and is expressed in μm^{-1}. We note that the astrometric 'pseudocolour' (Lindegren et al. 2018) was not used as it is much less precise than $\nu_{\rm eff}$ calculated from the BP and RP spectra.

3.4.2. Across-scan rate

The nominal scanning law of *Gaia* (see Gaia Collaboration et al. 2016, section 5.2) induces a periodic (~6 h) variation in the rate at which stellar images drift across the CCDs in the AC direction during integration (perpendicular to the TDI direction). The modulation is sinusoidal, and centred roughly on zero with an amplitude of approximately 177 mas s^{-1} or 1 AC pixel per second. The AC rate in angular units is denoted $\dot{\zeta}$ (the time derivative of the AC field angle ζ), however for the purposes of the PSF model we transform to units of pixels per second by dividing by the nominal AC angular pixel scale of 176.8 mas pixel^{-1}. In these units the AC rate is denoted $\dot{\mu}$. Although the in-flight pixel scale differs from the nominal value (by a different amount for each telescope), the nominal value is sufficiently close that a calibrated value is not required here.

The systematic difference between the image motion and the motion of the integrating charge packet causes a broadening of the observed PSF in the AC direction. For observations with the longest integration time (4.42 seconds, when no CCD gate is activated), the amplitude of the broadening is around 4.5 pixels. The strength of the effect varies enormously with the CCD gate length due to the differing integration times (see section 2), such that for gates 10 and shorter (corresponding to integration times

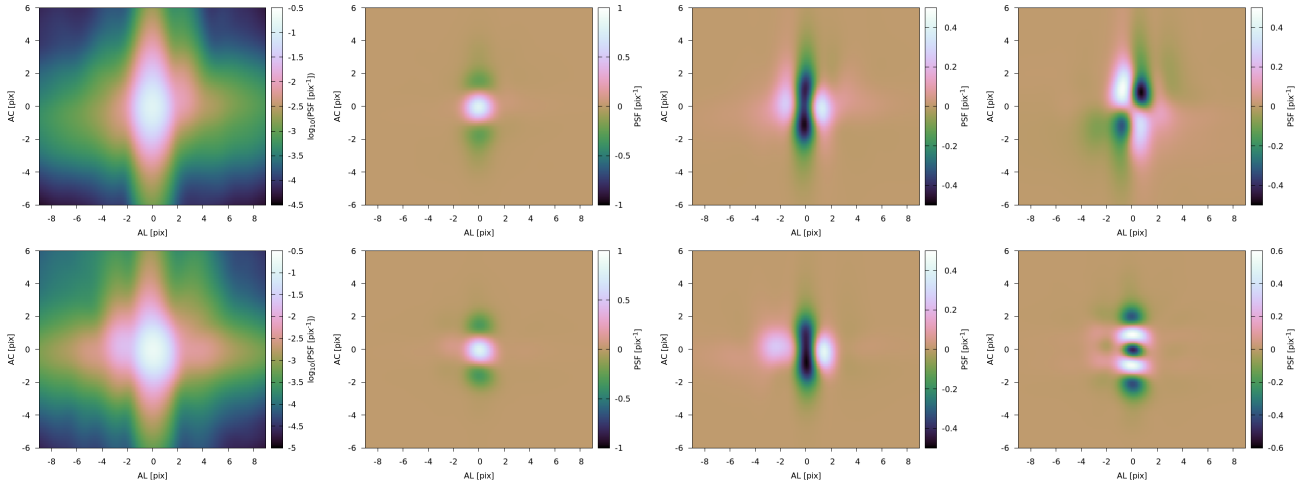

Fig. 4: Visualisations of the compound shapelets mean G_0 (column 1) and first three basis components G_1–G_3 (columns 2–4) for FOV1 (top row) and FOV2 (bottom row). Within each FOV the same components are used to model all CCDs. These demonstrate the large differences in the mean PSF between the two FOVs, but also the similarity in the low order basis components due to the PSFs for the two FOVs being subject to the same major dependences.

$\leq$ 1 second) the effect is negligible and the dependence is disabled in the model.

In principle, the effect of the broadening on the PSF should be invariant to the sign of the AC rate, and in *Gaia* DR2 the absolute value of the AC rate, $|\dot{\mu}|$, was used in the PSF model. However, it has since been discovered that small rotational misalignments of the CCDs cause the zeropoint of the broadening to be offset slightly from $\dot{\mu} = 0$. This phenomenon is known as 'native AC rate', and it induces a small asymmetry in the effect on the PSF that is nevertheless significant. This is accounted for in EDR3 by using the true value of $\dot{\mu}$, preserving the sign.

One important point to note is that because the broadening is strictly in the AC direction, the effect manifests only in the PSF observations and as such the LSF has no dependence on the AC rate. Although the scan law induces an analogous modulation in the AL image rate, it has a much smaller amplitude and the models developed for EDR3 assume that the AL rate matches the parallel charge transfer rate exactly such that no equivalent broadening effect is present in the AL direction (although see section 6.1 for some important consequences of this).

3.4.3. Across-scan position

The variation in the PLSF with position in the focal plane is to a large extent handled by calibrating each device independently. Within each device, the residual spatial variation manifests only in the AC dimension—because of the TDI mode in which *Gaia*'s CCDs are operated, the AL variation is marginalised and not directly observed. The AC coordinate on the CCD is denoted μ, and is a continuous value running from 13.5 to 1979.5 across the AC extent of the CCD image area. We note that in the geometric instrument calibration model (Lindegren, Lennart et al. 2020), the dependence on AC position is not continuous but split into nine segments that coincide with the CCD stitch blocks (arising from the manufacturing process; see Gaia Collaboration et al. 2016, figure 5). However, the PLSF is expected to vary smoothly with μ, and we model the dependence with a continuous function.

3.4.4. Model configuration

For EDR3 the spline configurations for all fitted observation parameters are presented in Tables 2–4. The configuration for the PSF model is different according to the CCD gate length, as explained above.

Table 2: Configuration for 1D LSF calibrations

Parameter	Units	Min	Max	Order	Knots
$\nu_{\rm eff}$	μm^{-1}	1.24	1.72	3	[-]
μ	pixels	13.5	1979.5	3	[-]

Table 3: Configuration for 2D PSF long gate (11, 12, 0) calibrations

Parameter	Units	Min	Max	Order	Knots
$\nu_{\rm eff}$	μm^{-1}	1.24	1.72	3	[-]
μ	pixels	13.5	1979.5	3	[-]
$\dot{\mu}$	pix·s^{-1}	-1.0	1.0	3	[-]

Table 4: Configuration for 2D PSF short gate (4-10) calibrations

Parameter	Units	Min	Max	Order	Knots
$\nu_{\rm eff}$	μm^{-1}	1.24	1.72	3	[-]
μ	pixels	13.5	1979.5	3	[-]

Each of the parameters $\nu_{\rm eff}$, μ, and $\dot{\mu}$ have typical values that are orders of magnitude different, and to improve numerical stability of the model they are normalised internally to the [-1:1] range. We note that the spline configurations for all three families of model are very simple, employing single-piece (no knots) third-order (quadratic) polynomials in each dimension. During development of the model with early versions of the *Gaia* pipelines and associated auxiliary calibrations, it was found that more complex configurations did not offer significant improvements to the PLSF reconstruction and could not be justified. This will likely be revised for future data releases as the data processing becomes more refined.

The multidimensional spline implementation adopted for use in this work has a number of free parameters $N_{\rm par}$ given by the order n_d and number of knots m_d in each dimension d, according to

$$N_{\rm par} = \prod_{d=1}^{D} (n_d + m_d)\,.$$

The PLSF basis components of different order all use the same spline configuration. Considering the number of basis components used in each model, the total number of free parameters in the PLSF models are listed in Table 5.

Table 5: Total number of free parameters for the LSF and PSF models ($N_{\rm total}$), which depends on the number of parameters per basis component $N_{\rm par}$ and the number of basis components $N_{\rm bases}$.

Model	$N_{\rm par}$	$N_{\rm bases}$	$N_{\rm total}$
1D LSF	9	25	225
2D PSF (long gates)	27	30	810
2D PSF (short gates)	9	30	270

3.4.5. Time dependence

The time dependence in the PLSF is very significant due to the changes in contamination level and telescope focus throughout the mission. The evolution over time is irregular, with large variations that are both smooth, during quiescent periods, and discontinuous, at decontaminations and refocuses. For these reasons it is impractical to calibrate the time variation in the same manner as the other dependences, by adding another dimension to the observation parameter space. Instead, the PLSF calibration is performed independently over 0.5-revolution steps, and the evolution of the calibration in time is solved incrementally by merging the independent calibrations using a square root information filter (Bierman 1977) implemented using Householder orthogonal transformations. A square root information filter is simply a method to solve the recursive least squares problem in a manner that is particularly numerically stable, because it does not square the design matrix to form the normal equations. It is similar to a Kalman filter but without the prediction step. This technique was pioneered during the Hipparcos data reduction (see van Leeuwen 2007, appendices C and D), and is referred to as a 'running solution'. An exponential decay constant of $\lambda = 80^{-1}$ revolutions is used to down-weight older solutions, which has the combined effects of smoothing out noise, enabling poorly constrained solutions to converge and allowing slow variations in time to be tracked. The filter 'lag' is eliminated by calibrating forwards and backwards in time then merging the solutions. The end result is that the solution at time t_0 is a weighted least squares estimate of the calibration parameters, where the statistical weight of the contributing data at time t has been reduced by a factor of $\exp(-\lambda|t - t_0|)$. The running solution is capable of tracking gradual changes in the PLSF profile but tends to smooth over discontinuities. For this reason, the solution is manually reset (the exponential weight function is truncated) at discontinuous changes in the PLSF calibration, such as at decontaminations and refocuses. Over the EDR3 time range there are five such events that require resets of the calibration for one or both telescopes. A list of these is presented in Table 6. The largest disturbances are the decontaminations, of which three occured during the EDR3 time range (a further three occurred during the commissioning phase, and the first in the EDR3 time range is number four).

Table 6: Resets of the PLSF calibration

OBMT [rev]	Event	FOV1	FOV2
1329.00	Decontamination #4	✓	✓
1443.96	Refocus		✓
2342.00	Decontamination #5	✓	✓
2574.65	Refocus	✓	
4124.00	Decontamination #6	✓	✓

4. Calibration pipeline

The PLSF calibration pipeline developed for EDR3 involves a series of procedures that ultimately solve for the parameters of the PLSF models over the whole mission time and for all calibration units. The procedures vary in complexity and differ according to whether or not they can be parallelised in time, which impacts the implementation and execution plan. Automated validation algorithms are used to ensure that the ~10^7 different solutions meet some predefined quality criteria that guarantee their fidelity. The products of the pipeline are distributed to downstream consumers within the *Gaia* Data Processing and Analysis Consortium who require the PLSF calibration for various higher level data processing tasks. In this section, we describe the calibration pipeline stages and discuss some important aspects of the design.

4.1. Observation preprocessing

The PLSF pipeline follows the self-calibration principle of the *Gaia* data processing (Gaia Collaboration et al. 2016, section 3.1), which means in practice that the observations used to calibrate the PLSF are a subset of the regular science observations and no special calibration data is required. However not all observations are suitable for use in the PLSF calibration, and those that are must be carefully selected and prepared. In this section we describe these preprocessing steps.

4.1.1. Eligibility of observations

Each transit observed by *Gaia* provides observations in nine (CCD row 4) or ten (CCD rows 1–3,5–7) successive CCD strips, and thus may be eligible for use in calibrating up to ten independent PLSF calibration units. However, not all observations are suitable, and we define eligibility criteria at both the transit-level and the strip-level. Transits that are eligible for use in the PLSF calibration must have a valid $\nu_{\rm eff}$, a valid astrometric solution, and an astrometric excess noise below 0.5 mas. These imply that the transit must have been successfully cross-matched to a known *Gaia* source (as described in Torra, Ferran et al. 2020). As the PLSF pipeline is one of the first to run in the data processing cycle (after the cross-match and several lower level CCD calibrations), the photometry and astrometry necessarily come from the previous data processing cycle, specifically from the outputs of the PhotPipe and AGIS systems (see Riello et al. 2020; Lindegren, Lennart et al. 2020). This risks propagating systematic errors from one cycle to the next, and during the processing for EDR3 an additional iteration with AGIS was performed in order to mitigate this.

We note that the photometric quantity $\nu_{\rm eff}$ is the mean value and not the epoch value computed from the individual transit.

The mean value is more precise, although it may be inaccurate for sources that have significant variability. Most of the variable sources will be removed as outliers during later stages of the PLSF calibration pipeline. The $\nu_{\rm eff}$ is needed in order to calibrate the colour dependence in the PLSF, and provides one of the observation parameters (see section 3.4).

The astrometric solution is used in conjunction with the attitude and geometric instrument calibration to predict the location of each source in the observed pixel stream, and to supply values for the AC rate of the observation. The predicted locations are used to align the set of observations that are eventually used to solve the PLSF calibration. We note that this is a significant departure from more traditional PSF calibration methods, which would refine an initial empirical estimate of the source location iteratively with the PSF solution. There are a number of important reasons for this. Firstly, the *Gaia* observations are rather undersampled, such that most empirical location estimators are biased and risk introducing systematic errors in the PLSF calibration. Secondly, there is a close coupling between the PLSF calibration and the global astrometric solution computed within AGIS (which includes the attitude and geometric instrument calibration). Using predicted locations allow for consistency between the locations defined within AGIS and those adopted by the PLSF. Finally, the use of predicted locations allows effects that shift the PLSF centroid without any change in the source location, such as chromaticity, to be calibrated directly in the PLSF. This permits a greater separation of roles between the PLSF calibration and global astrometric solution.

For transits that pass the transit-level criteria, the following strip-level criteria are applied, mainly to reject observations that have been compromised in one way or another by the complex way in which the *Gaia* CCDs are operated. The sampling and windowing strategy, and its interaction with the gating, charge injection and other processes that are not synchronised between the CCD strips, can result in transits for which only a subset of the strip-level observations are used. Observations in each CCD strip that are eligible for use in the PLSF calibration must have a single CCD gate (that is the expected one given the source magnitude), nominal window geometry, no charge injection present within 50 TDI of the window, a predicted location that is consistent with the empirical location (derived from the centre-of-flux), and a profile that is consistent with that of a fixed reference PLSF calibration. The first of these criteria arises because faint stars that are wholly or partially coincident in the AL direction with a bright star will be observed wholly or partially with the gate appropriate for the bright star. As such, they will have a PLSF profile that is of very low signal to noise, or otherwise compromised by anomalies associated with the activation and deactivation of the CCD gate—different samples in the profile will have different integration times and sample different AL regions of the CCD. The requirement on the window geometry is necessary due to the truncation of overlapping windows that occurs when two sources are very close together, such that the assigned windows are in conflict (see Fabricius et al. 2016, section 2). The restriction on the charge injection distance is intended to exclude observations containing a significant flux contribution from released charge in the pixels close to the charge injection. The final two criteria are used to reject observations that have poor predicted locations or PLSF profiles that are significant outliers. The majority of these are close pairs that have not been detected as such. The reference PLSF calibration that is used in this step is discussed further in section 6.4.

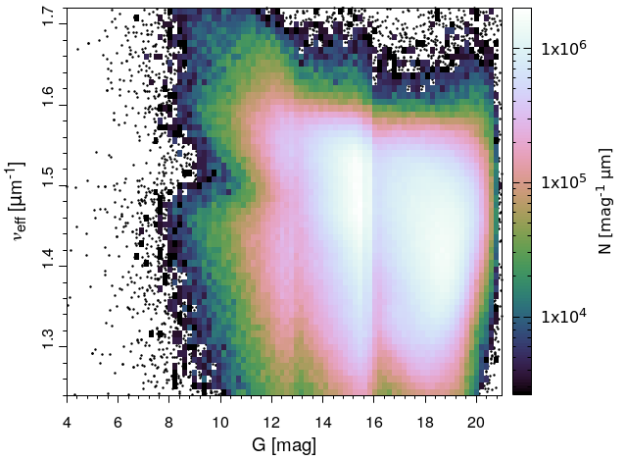

Fig. 5: Distribution in the (G, $\nu_{\rm eff}$) plane of 1604769 eligible observations that have passed the first stage of selection.

4.1.2. Selection of observations

Observations that pass the eligibility criteria then undergo two stages of selection for use in the PLSF calibration. In the first stage, all eligible observations are selected from the data stream uniformly in time up to a limit of 1000 per hour of mission time and per calibration unit, although only the calibration units corresponding to faint observations reach this limit. The main purpose of this stage is to throttle the number of observations and reduce memory overheads. This provides many more observations than are necessary to formally constrain the PLSF model, however the need to adequately constrain the solution over the whole observation parameter space implies that a large number of objects must be made available to the calibration.

The second stage involves selecting observations uniformly within the PLSF observation parameter space, particularly in the $\nu_{\rm eff}$ and $\dot{\mu}$ dimensions, in order to fully constrain the model over the whole range. The distribution of observations within the parameter space is highly non-uniform and certain regions, such as extreme colours, are very sparsely populated. It is important that the density of objects used in the calibration is balanced across the parameter space, to ensure that the PLSF model is well constrained even for rare types of object.

To demonstrate this, Figure 5 shows the distribution in the (G, $\nu_{\rm eff}$) plane of 1604769 eligible observations that have passed the first stage of selection. These were observed on CCD row 1 over eight revolutions from 4020–4028. The step changes at $G = 13$ and $G = 16$ correspond to the boundaries between different window classes. The $\nu_{\rm eff}$ distribution is highly non-uniform and varies significantly with magnitude. Figure 6 shows how the same observations are distributed in the ($\dot{\mu}$, $\nu_{\rm eff}$) plane. The mean $\nu_{\rm eff}$ of sources on the sky is a function of Galactic latitude, which results in a correlation between $\nu_{\rm eff}$ and AC rate that varies over time. As a consequence of this, the PSF joint dependence on $\dot{\mu}$ and $\nu_{\rm eff}$ cannot be fully constrained over short time ranges. Finally, Figure 7 depicts the time variation in the AC rate, which follows the planned scan law closely (see Gaia Collaboration et al. 2016, section 5.2) with minor departures due to various small disturbances. The AC rate varies sinusoidally with a period of 1 revolution, an amplitude of around 1 pixel per second, and is out of phase between the two telescopes by 106.5° (the basic angle). The strong time variation in AC rate implies that the PSF calibrations with a dependence on this parameter (see Ta-

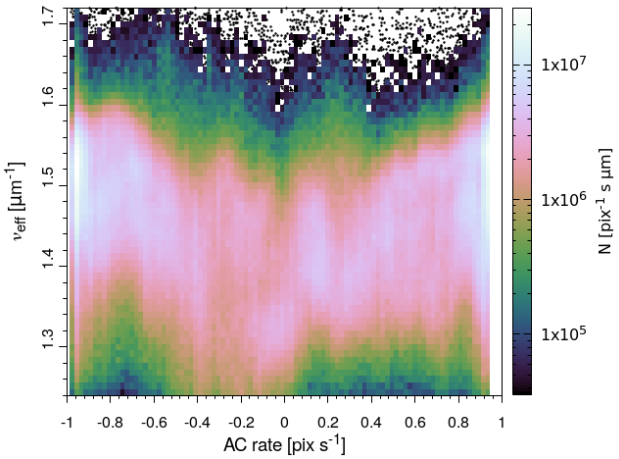

Fig. 6: Distribution in the ($\dot{\mu}$, $\nu_{\rm eff}$) plane of the observations depicted in Figure 5. There is a correlation between $\dot{\mu}$ and $\nu_{\rm eff}$ that evolves over time (see text).

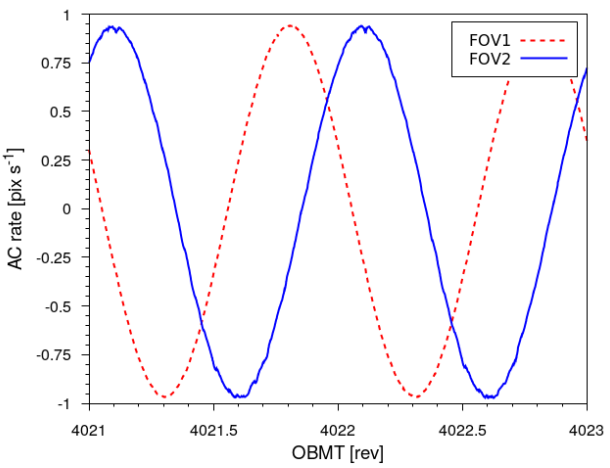

Fig. 7: Time variation in AC rate for observations in each telescope.

ble 3) require at least half a revolution to be fully constrained—although the correlation with $\nu_{\rm eff}$ and the sparsity of observations at extreme values of $\nu_{\rm eff}$ mean that in practice a larger time range is required.

Considering these factors, when making the final selection of observations to be used in the PLSF calibration we define a uniform grid in the observation parameter space and select one object per bin until either the grid is fully populated or the observations have run out. This is done separately for each calibration unit and in steps of 0.5 revolutions, over which the independent PLSF solutions are computed—see section 4.2. The grids used are configured such that the individual 1D LSF solutions can have up to 4000 observations sampled uniformly in ($\nu_{\rm eff}$, μ), and the PSF calibrations can have up to 125 observations sampled uniformly in ($\nu_{\rm eff}$, μ, $\dot{\mu}$), although the grids are rarely fully populated. The difference in total number of observations is due to the fact that each 1D observation used to constrain the LSF supplies 12 or 18 samples for use in the fit, whereas each 2D observation used to constrain the PSF supplies 216 (for AF2–9) or 108 (for AF1).

4.1.3. Preparation of observations

The observations selected for use in the PLSF calibration must be carefully prepared. First, observations are converted from analogue-to-digital units (ADU) to electrons by multiplying by the analogue-to-digital converter (ADC) gain level. Then, each observation is corrected to remove the electronic bias, background and dark signal. Each of these steps relies on auxiliary calibrations of the associated effect that are computed by the data processing pipelines that run prior to the PLSF pipeline. The electronic bias combines the bias prescan level, which is constant for all samples in an observation although it varies slowly in time (see Fabricius et al. 2016, section 5.1.1), and bias non-uniformity, which can vary from sample to sample and has a complex dependence on the CCD readout sequencing as described in Hambly et al. (2018). The background is dominated by stray light due to the compact, folded design of the optical system, but also includes a minor component arising from charge release into the pixels behind a charge injection, although by excluding observations in the first 50 TDI lines following a charge injection this component is negligible. The background model has been completely redesigned since DR2 in order to better reproduce sharp stray light features, and is described in section 3.3.4 of Gaia Collaboration (2020).

Next, each sample is assessed to determine if it is affected by a range of defects including saturation, non-linearity, cosmic rays, and various CCD cosmetic defects such as dead and hot columns. These in turn rely on further auxiliary calibrations of the CCDs that are determined ahead of the PLSF pipeline (see Hobbs et al. 2018, section 2.3.4). This information is distilled into a sample mask that defines which of the samples are suitable for use. Additionally, for the SM observations (which use much longer windows in the AL direction) we mask off samples in the far wings such that only the central eight (WC1) or four (WC2) AL samples are used. The motivation for this is that the samples in the far wings have very low signal to noise and are more likely to be compromised by secondary sources.

The resulting unmasked samples must then be normalised to match the constraints of the PLSF models, which require that the flux falling in the unobserved region outside of the window area (the enclosed energy fraction) is accounted for—in both the AL and AC direction in the case of the PSF model, and in just the AL direction in the case of the LSF model. In principle this could be done by incorporating the photometric calibration in order to estimate the total instrumental flux of the observation, given the calibrated magnitude of the source (which is available from the cross-match). Comparison with the observed number of electrons in the window would then provide the appropriate normalisation factor. However, due to restrictions arising from the overall DPAC pipeline design and the formulation of the photometric calibration this method is not feasible. Instead, a static reference PLSF calibration is used to fix the enclosed energy fraction to a nominal value. The reference calibration has no time dependence, but includes all calibration units and models the colour, AC position and AC rate dependences so that the enclosed energy fraction has a physically reasonable value. This results in observations that are normalised sufficiently accurately to allow the PLSF solution to stabilise, at the expense of losing some sensitivity to genuine changes in the enclosed energy fraction over the course of the mission. This procedure is somewhat ad hoc, and may be revised substantially for future data releases as the data processing systems become more refined. This is discussed further in section 6.4.

The uncertainties on each sample are estimated by combining the shot noise, readout noise and uncertainties on the associated auxiliary calibrations (bias, background and dark signal). An additional contribution is added to account for the uncertainty on the predicted location of each observation, in order to down-weight observations with noisier locations. This is done by propagating the location error (in TDI) to the corresponding error on the (normalised) samples by multiplying it by the gradient of the PLSF at the location of the sample. Once again the static reference PLSF calibration is used to estimate this. For 2D observations both the AL and AC location uncertainties are included. This makes a larger contribution in steeper regions of the profile where the effects of uncertainty on the location are more significant. The various terms that contribute to the estimated sample uncertainties are unlikely to be fully independent and may in some cases be poorly estimated, highly non-Gaussian, or correlated between the samples. As a result, the estimated sample uncertainties are likely to be somewhat biased, which has implications for the interpretation of the statistics of the PLSF model fit. However, they provide suitable values for use in weighting the samples used in the fit.

4.2. Partial solution

The solution for the PLSF model parameters is computed independently for each calibration unit and in steps of 0.5 revolutions. For the 1268 calibration units and 4152 revolutions covered by EDR3 data, this amounts to 10,529,472 individual solutions. These are referred to as 'partial solutions' because for many calibration units there are insufficient observations to fully constrain the parameters.

The PLSF model parameters that must be solved correspond to the parameters of the spline functions that are used to interpolate the basis component amplitudes (h_n and g_m in Equations 1 and 4). Using the LSF model as an example, the spline value h_n can be represented as the inner product of the P spline parameters $\boldsymbol{a}^T = [a_1, a_2, \ldots, a_P]$ and the spline coefficients $\boldsymbol{y}(\boldsymbol{o})^T = [y(\boldsymbol{o})_1, y(\boldsymbol{o})_2, \ldots, y(\boldsymbol{o})_P]$ so that

$$h_n = \boldsymbol{a}^T \boldsymbol{y}(\boldsymbol{o}) \,. \tag{5}$$

The spline coefficients $\boldsymbol{y}$ are functions of the observation parameters $\boldsymbol{o}$, where $\boldsymbol{o} = [\nu_{\rm eff}, \mu]$ or $\boldsymbol{o} = [\nu_{\rm eff}, \mu, \dot{\mu}]$ depending on the PLSF model (see Tables 2–4). Each basis component uses the same spline configuration and so has the same number of parameters that are solved jointly. The full set of parameters can be represented in a single column vector $\boldsymbol{x}$ as follows

$$\boldsymbol{x}^T = [\boldsymbol{a}_1^T, \boldsymbol{a}_2^T, \ldots, \boldsymbol{a}_N^T] \,, \tag{6}$$

where $\boldsymbol{a}_n$ contains the spline parameters corresponding to basis component n. The parameter vector $\boldsymbol{x}$ can be expressed in a system of linear equations

$$A\boldsymbol{x} = \boldsymbol{b} \,, \tag{7}$$

where the observation vector $\boldsymbol{b}$ contains all the samples of the selected observations, preprocessed as described in section 4.1.3 and after further subtraction of the PLSF mean. As the amplitude of the mean is fixed at 1.0 it is excluded from the fit, and only the amplitudes of the basis components are solved for by fitting to the sample residuals. The observation vector $\boldsymbol{b}$ can be written as $\boldsymbol{b}^T = [\boldsymbol{s}_1^T, \boldsymbol{s}_2^T, \ldots, \boldsymbol{s}_J^T]$ where $\boldsymbol{s}_j$ represents the K samples from observation j, and $\boldsymbol{s}_j^T = [s_j^1, s_j^2, \ldots, s_j^K]$ where s_j^k represents the $k^{\rm th}$ sample from the $j^{\rm th}$ observation. The rows of the design matrix A are composed as

$$[H_1(u_j^k)\boldsymbol{y}^T(\boldsymbol{o}_j), H_2(u_j^k)\boldsymbol{y}^T(\boldsymbol{o}_j), \ldots, H_N(u_j^k)\boldsymbol{y}^T(\boldsymbol{o}_j)]$$

where $H_n(u_j^k)$ represents the value of basis component n at the location u of the sample s_j^k. Finally, the error on each sample σ_s is used to weight the entries in the observation vector and design matrix, by dividing the corresponding element in $\boldsymbol{b}$ and row in A by σ_s. Although the LSF model has been used as an example here, the equations extend naturally to the PSF model and the same methods are used to solve for the PSF parameters.

The partial solution is obtained by applying Householder orthogonal transformations to Equation 7 that reduces matrix A to a particular upper triangular form. For further details, see van Leeuwen (2007, appendix C) and Bierman (1977).

4.3. Running solution

The partial solutions from independent half-revolution time steps contain noise, may in some cases not have a unique solution due to fewer observations than parameters, and in most cases are not well constrained over the whole observation parameter space due to a lack of objects in certain regions. In order to reduce noise and improve the constraint, while tracking gradual time evolution in the PLSF calibration, the partial solutions are combined using the running solution methodology described in section 3.4.5. In effect this produces an updated solution for each half-revolution time step, that is a merger of many earlier and later partial solutions weighted according to the time difference.

4.4. Data gaps

At certain periods throughout the EDR3 time range there may be no observations available to constrain the partial solution for some or all of the calibration units. This may happen by chance for bright calibration units for which stars in the magnitude range are rare. This also happens at times due to anomalies on the satellite, problems during the downlink of data, or transient issues affecting the various auxiliary calibrations that are required to prepare the PLSF inputs. Observations can also be excluded by design, for example during each decontamination when the collection of science data is halted, and for a short time afterwards while the instrument is still thermally unstable.

During these periods, the PLSF pipeline still runs but the partial solution produced is that of the identity solution. This carries no weight in the running solution, such that the running solution is simply propagated over the gap in the data with no change. This ensures that there is always a well-constrained PLSF calibration available, for example to process science observations that are present but that did not meet the requirements for use in the PLSF pipeline.

4.5. Autoqualification and outputs

The scale of the data processing and calibration task, with more than ten million calibrations each of which solves the amplitudes of tens of basis components over a two or three dimensional parameter space, necessitates the use of automated qualification and validation algorithms to monitor the integrity of the calibration pipeline. These are under constant review and development as the PLSF models evolve and our understanding of the data improves.

At the lowest level, these amount to verifying that certain parameters are within allowed ranges and that undefined values have not entered the calibration. Gaps in the input observations are detected and checked against known mission events (e.g. Boubert et al. 2020). The statistics of the PLSF fits are tracked to reveal any time ranges or subsets of the calibration where the models cannot reproduce the observations as accurately as expected. For every individual calibration, the PLSF solution is inspected at a range of points within the observation parameter space in order to check its integrity. Invalid PLSF solutions are those for which the average basis component amplitudes exceed a threshold, or those for which the reconstructed PSF or LSF goes significantly negative or has a large number of local maxima. Some margin is necessary to account for the fact that the PLSF solution is produced by a calibration to noisy data, and as such may contain minor unphysical features that do not necessarily indicate a problem with the pipeline.

Ideally, with PLSF models incorporating all known physical effects, accurate auxiliary calibrations and properly characterised error distributions, all PLSF solutions would pass autoqualification and be approved for use. However, with EDR3 this situation has not yet been reached, and there are some subsets of the calibration units that have not been adequately calibrated, as explained in section 5.3. Any solution that fails autoqualification must be replaced with a suitable alternative, which invariably means either copying a solution from the same calibration unit at a different time, or copying the solution from a different calibration unit for which the PLSF solution is expected to be similar.

For every half-revolution period, the full set of calibrations for the whole focal plane are compiled into a single product for distribution to downstream consumers within the *Gaia* DPAC. Each such PLSF 'library' is roughly 4.9MB in size, rising to ~570MB when the covariance information on the PLSF parameters is included; the total size of the pipeline products is therefore ~4.7TB.

4.6. Implementation and execution

The PLSF models and calibration pipeline are implemented in the Java programming language as part of the *Gaia* DPAC codebase. Within the overall DPAC architecture the PLSF calibration pipeline forms part of the CALIPD processing system that is referred to in other DPAC publications. CALIPD combines the instrument calibrations (CAL), which include the PLSF, and the IPD. The PLSF calibration is broken into a series of six modules that are executed in series and which each perform a different stage of the pipeline: observation preprocessing, partial solution computation, forwards- and backwards-in-time running solutions, solution merger, and output assembly and packaging. The running solution and output assembly tasks must be executed sequentially by time, whereas the other tasks can be parallelised by time. Tasks can also be parallelised by calibration unit for further optimisation, with the overall architecture being tailored towards the execution environment.

The execution of the PLSF calibration is done at the Data Processing Centre, Barcelona (DPCB), in particular at the MareNostrum supercomputer hosted by the Barcelona Supercomputing Center (BSC). Because of the machine design the use of databases is discouraged, and instead a hierarchical file system was used for hosting the raw data and intermediate products. The MareNostrum resources are not exclusively dedicated to *Gaia* and the access is through job submission to a shared queue. Consequently, the PLSF calibration has been developed with batch processing in mind. This decision was largely based on the nature of the majority of DPAC tasks executed at DPCB, where a lot of data has to be processed by loosely coupled tasks. Batch processing is very efficient in processing high volume data, where data is collected, entered to the system, processed and then results are produced in batches. The use of partitioning allows multiple jobs to run concurrently, thus reducing the elapsed time required to process the full data volume. Special care must be taken in the partitioning of jobs to exploit the available resources efficiently. In total, the execution of the PLSF calibration pipeline for EDR3 consumed around 430,000 CPU hours and required around 66TB of storage for the outputs and intermediate products. Figure 8 depicts the distribution of resources among the pipeline stages.

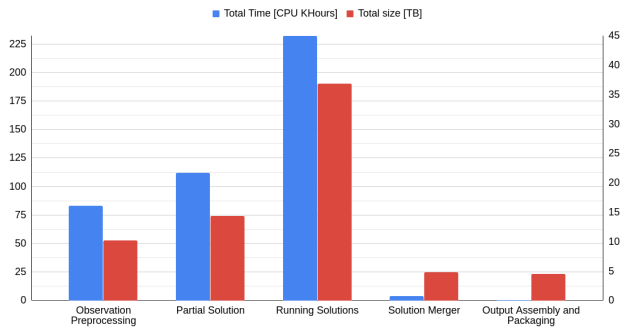

Fig. 8: Performance of the PLSF calibration pipeline implemented for EDR3 in terms of the resource consumption (CPU hours and disk space) by different stages of the pipeline.

4.7. Image parameter determination

As an aside, it is useful to the reader to briefly describe how the PLSF calibration is actually used in the *Gaia* data processing. Further details can be found in section 3.3.6 of Gaia Collaboration (2020). Within the overall *Gaia* processing chain, the PLSF models are used as part of the pre-processing of the raw data that aims to determine, for every window, the basic observables (or 'image parameters') of location (in the pixel data) and flux. Every window is assumed to contain exactly one point source. The image parameters form the primary inputs to both the astrometric and photometric (G band) calibrations described in other papers. This IPD relies on numerous auxiliary calibrations in addition to the PLSF. After debiasing, the window samples are fitted with a model consisting of the sum of a LSF (or PSF for 2D windows) and a constant background offset. The PLSF solution is selected according to the FOV, device, CCD gate and time of the window, and is configured with the $(\nu_{\rm eff}, \mu, \dot{\mu})$ parameters of the observation (a default value is adopted for $\nu_{\rm eff}$ if not known). The image parameters that are solved for are the location (AL only for 1D observations, or AL and AC for 2D observations), instrumental flux and the background offset. The background offset is a nuisance parameter that is fitted in order to better handle sharp features in the stray light variation. The fitting is performed using a maximum likelihood algorithm described in Lindegren (2008). The adopted 'centre' of a star is defined by the origin of the PLSF model, which itself is aligned with the predicted locations of the observations used to calibrate the model. These are supplied by the astrometric solution. This circularity leads to a degeneracy between the PLSF origin and the geometric part of the instrument calibration (performed within AGIS), which future data releases will aim to resolve (see section 6.7.2). The assumption of

a single point source is obviously a simplification, and within DPAC there are subsystems dedicated to the processing of extended objects and non-single-stars, although these results are not part of EDR3.

5. Results

In this section we present some results of the calibration. During the processing for EDR3, two iterations of the PLSF and AGIS calibrations were performed in order to improve the convergence and reduce some systematic errors present in the first iteration. The outputs of the second iteration provided the inputs used to compute the final EDR3 data products, and it is the results of this second PLSF calibration that are presented here.

Given the size, complexity and dimensionality of the PLSF calibration products, it is not feasible to present everything and care is required in order to distill the results into a meaningful set of analyses. We present a selection of results from specific subsets of the calibration that are carefully chosen to demonstrate certain key aspects, and which are representative of the calibration as a whole. In many cases the along-scan full-width-half-maximum (AL FWHM) is used to quantify the image sharpness, reveal gradual evolution in the instrument, and provide a proxy for the relative astrometric constraint.

5.1. Time evolution

In Figure 9 we present the mean AL FWHM over all AF2-9 1D calibrations, for each FOV separately, and over the whole EDR3 time range. AF1 devices, which use a different window length, are excluded to maintain consistency in the inputs. The vertical lines mark the times at which the calibration running solution (section 3.4.5) is reset due to a major mission event (see Table 6). These include decontaminations (solid lines), and refocusses of FOV1 (dashed line) and FOV2 (dot-dashed line). The time evolution thus corresponds to a gradual degradation in the image sharpness due to slowly changing instrument focus, punctuated by step changes. The rate of degradation is higher earlier in the mission: The payload has become more stable throughout the years, which manifests in other effects such as slower rates of mirror contamination. After the sixth decontamination at revolution 4124 the degradation in image sharpness is very modest, and at the time of writing (revolution ~9800) there have been no more decontaminations and the image quality has been maintained by refocussing alone.

After each decontamination *Gaia* takes some time (typically a few tens of revolutions) to reach thermal stability, and the evolution of the PLSF is quite rapid during this period. Figure 10 shows a zoom-in of the time range immediately after the reset of the PLSF running solution following decontamination five at revolution 2342. In this figure the AL FWHM obtained from the running solution (lines) is compared with that obtained from the partial solution (points), which provides a calibration of the instantaneous instrument state. The rapidly improving image sharpness as the instrument cools cannot be accurately tracked by the running solution, due to the way in which it merges solutions over a wide time range. This leads to a systematic difference between the true PLSF and the calibrated solution for a short period after each decontamination. Ways to mitigate this in future data releases are discussed in section 6.5.

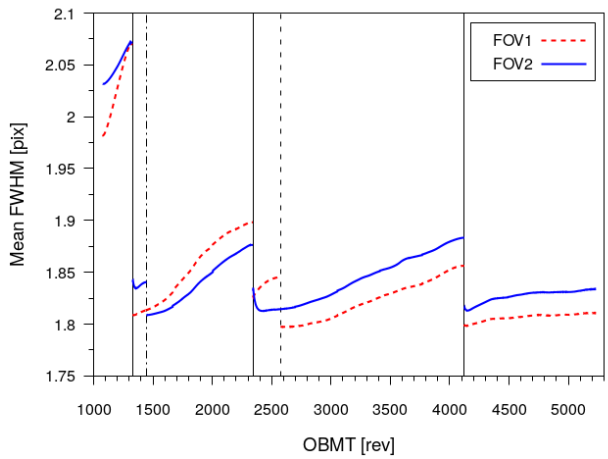

Fig. 9: Time variation in mean AL FWHM of the AF2-9 WC1 calibrations, for FOV1 (dashed red line) and FOV2 (solid blue line). The vertical lines mark decontaminations (solid line) and refocusses of FOV1 (dashed line) and FOV2 (dot-dashed line). These coincide with resets of the calibration running solution.

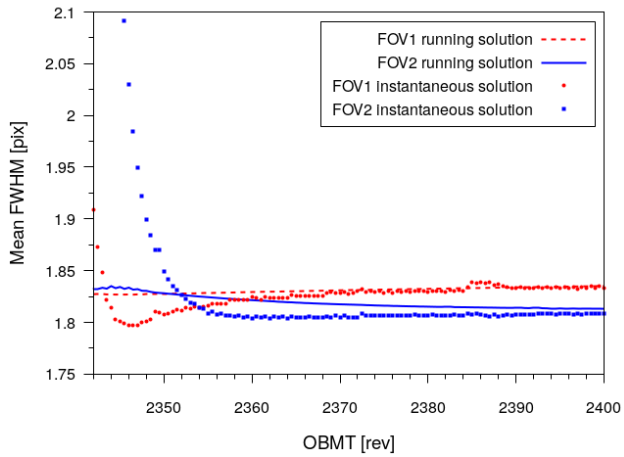

Fig. 10: Zoom-in of Figure 9 showing the period shortly after the fifth decontamination when the instrument is cooling and the PLSF is evolving rapidly. In this situation the running solution (solid lines) diverges from the partial solution (points).

5.2. Colour, AC position, and AC rate dependence

At each instant in time the PLSF dependences on colour, AC position, and AC rate are calibrated. The effects of variation in source colour are depicted in Figure 11, where the mean of the calibrated AL profiles for different values of the effective wavenumber $\nu_{\rm eff}$ are shown. The two FOVs present quite different AL profiles due to the different wavefront errors between the two telescopes, with the first diffraction peak appearing on opposite sides of the central maximum. This overall form is present throughout the entire time range and for the PSF as well. The variation with source colour manifests through the strong dependence on $\nu_{\rm eff}$; as expected, smaller values of $\nu_{\rm eff}$ (which correspond to longer effective wavelengths) resulting in broader profiles with stronger diffraction features.

The dependence on AC position is depicted in Figure 12, which shows the variation in AL FWHM across the entire AF instrument for each FOV separately, obtained from the WC1 (LSF)

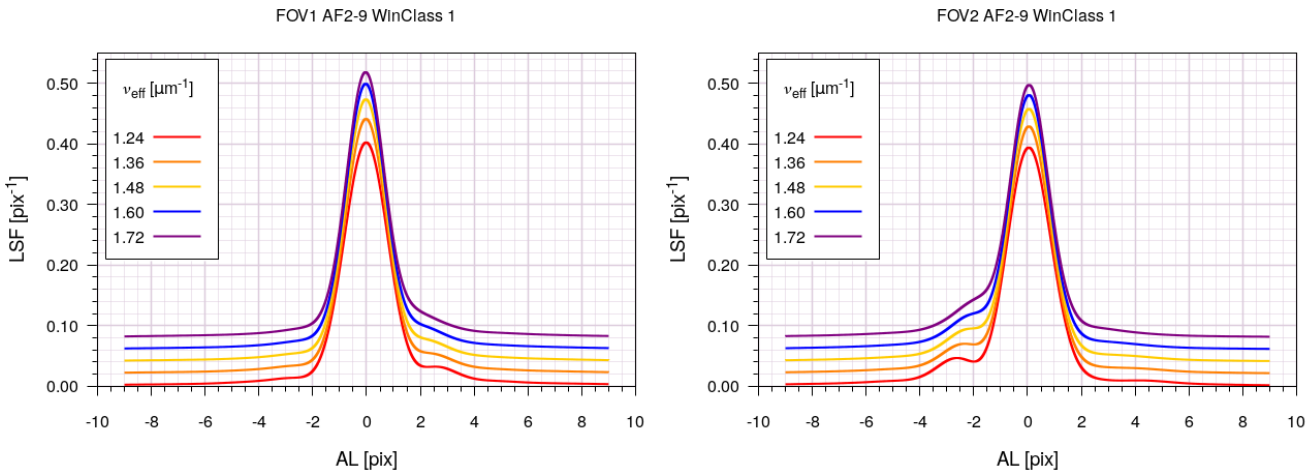

Fig. 11: Colour variation for the AF2-9 WC1 LSF for FOV1 (left) and FOV2 (right). The profiles have been offset vertically by 0.02 for clarity. There is a clear trend with profiles for larger effective wavenumbers being sharper with less obvious diffraction features in the wings.

calibrations at revolution 3343 and for $\nu_{\rm eff} = 1.43\mu{\rm m}^{-1}$. The 62 CCDs that comprise the AF instrument are shown at true relative size and position. In principle, the profiles are expected to be sharper closer to the optical centre and to vary smoothly across the focal plane, and this is indeed reflected in the calibration, which solves each device independently and does not enforce these properties *a priori*. For both FOVs there is a clear degradation of the image sharpness towards the corner of the focal plane at CCD row 7 and strip AF1, a feature well established since the commissioning phase (Busonero et al. 2014). The evolution is not completely smooth across the focal plane, and some devices show small discontinuities with their neighbours. These could be due to a general lack of constraint towards the edge of the CCDs, issues with the auxiliary calibrations, or minor unmodelled electronic effects that depend on the AC position. There are also two CCDs, AF5 and AF8 in row 2, that have exceptionally good image sharpness in both FOVs. Examination of observations in these devices indicates that the change in PSF shape is genuine and not an artefact of the calibration. The fact that both FOVs are affected suggests that the root cause lies with the CCDs and not the optical part of the PSF. These two devices have also been found to have lower quantum efficiency than the other AF CCDs, with a depressed sensitivity at redder wavelengths, which could explain the difference in PSF.

The variation with AC rate manifests only in the PSF, and leads to a broadening in the AC direction as the stellar image moves during integration. The strength of the dependence varies according to the CCD gate, as explained in section 3.4.2, with gate 0 having the strongest dependence. In Figure 13 we present a selection of calibrated PSF models for different values of the AC rate (0.0, 0.6 and 1.0 pixels per second, from left to right) and for FOV1 (top row) and FOV2 (bottom row). These are taken from the CCD row 4, strip AF5, gate 0 calibration at revolution 4400. They clearly demonstrate the broadening effect on the PSF for non-zero values of AC rate. The slight bimodality in the PSFs at high AC rate (right panels) is an artefact of the calibration that has been studied extensively since the EDR3 calibrations were computed. This is discussed in detail in section 6.1.

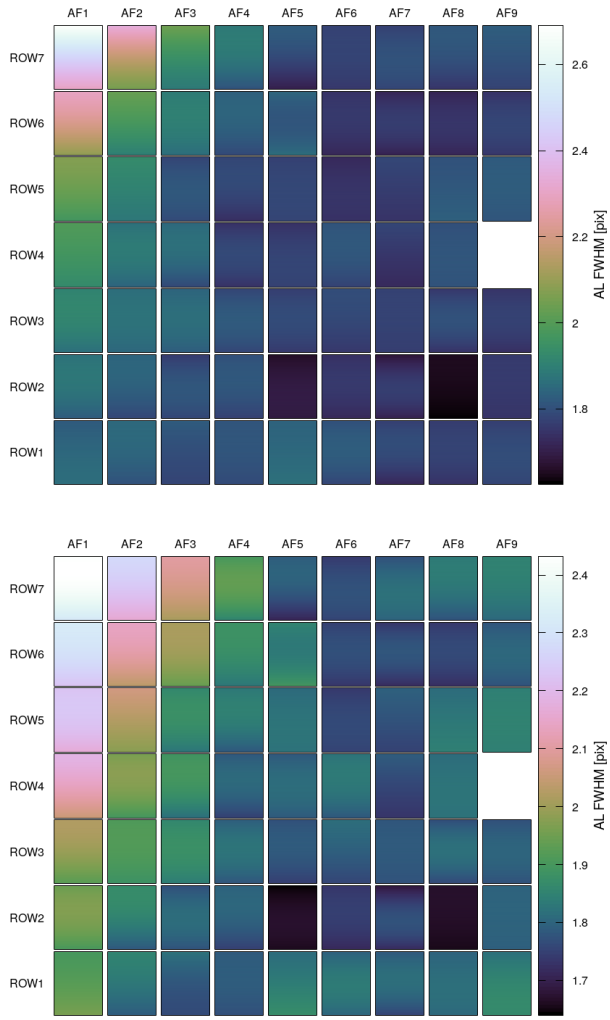

Fig. 12: Variation in the AL FWHM with AC position within each CCD and across the AF focal plane, for FOV1 (upper panel) and FOV2 (lower panel). Obtained from the calibration at revolution 3343 and for $\nu_{\rm eff} = 1.43\mu{\rm m}^{-1}$.

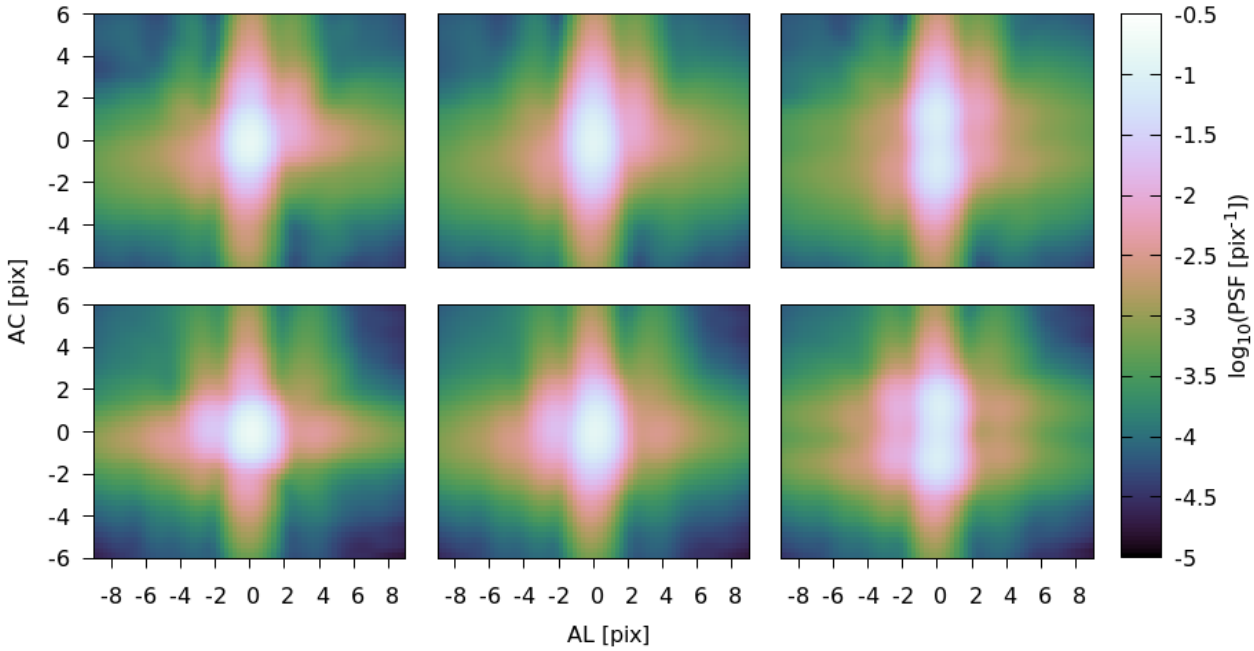

Fig. 13: AC rate ($\dot{\mu}$) variation for the FOV1 (top row) and FOV2 (bottom row) calibrations for CCD row 4, strip AF5, gate 0. The plots correspond to AC rate values of 0.0 (left), 0.6 (middle), and 1.0 (right) pixels per second. See the text for details.

5.3. Invalid solutions

The autoqualification and validation criteria described in section 4.5 are not met by all subsets of the calibration. Specifically, the calibrations for SM CCDs and AF WC2 observations fail various thresholds and have not been qualified for use. It is for this reason that the SM and AF WC2 calibrations are not included in the results presented in this section. In both cases, the solutions for these calibration units are discarded and replaced with qualified solutions from other calibrations, as explained below.

The SM calibrations for both WC0 and WC1 are complicated by numerous differences in the data compared with similar AF observations. These include the use of a fixed CCD gate (12) that does not adapt to the magnitude of the source (leading to WC0 observations heavily affected by saturation), on-chip binning (by 2x2 pixels for WC0 and a further 2x2 binning in software to 4x4 pixels for WC1) that results in a highly undersampled PSF, higher ADC readnoise (of ~10.8 e^- compared to ~4.3 e^- for AF2-9 strips, see Hambly et al. (2018)), and the fact that the SM PSF has quite a different form to AF due to being further from the optimum wavefront location. The final issue causes problems with the PSF model because the basis components are tailored towards AF observations. In addition, the PSF model has problems reproducing gate 12 observations (see section 6.1) that further destabilise the fit. Many of these issues also have an impact on the various auxiliary calibrations that the PLSF calibration relies on. In particular, the geometric instrument calibration for SM is noisier, which results in noisier predicted locations for each observation. Each SM PSF solution is therefore discarded and replaced with the solution from the AF2 strip with the same CCD gate, row, FOV, and mission time. This choice was judged to be a good compromise between minimising spatial variations in the PSF while maximising the solution stability. This procedure is not ideal and major effort has been spent on resolving these various problems in order to achieve an independent calibration of the SM PSF for future *Gaia* data releases (see section 6.7). However, we also note that in *Gaia* EDR3 the SM observations have not been used in the astrometric or photometric solutions for sources, and as such the SM calibrations are of lower importance to AF.

The AF WC2 calibrations suffer mainly from low signal to noise in the observations. Also, for these faint observations the stray light background is more significant, and uncertainties in the background calibration affect the solution to a greater extent. The solutions for the AF WC2 calibrations are therefore discarded and replaced with the solution for the WC1 calibration in the same device, FOV and mission time. Being coincident in the focal plane, the linear part of the LSF is expected to be identical between WC1 and WC2, with any differences limited to signal-level dependent effects that are in any case not included in the LSF model at this point.

5.4. Fit statistics and calibration residuals

In Figure 14 we present the evolution of the PLSF model reduced chi-square statistic χ^2/ν over the EDR3 time range, as a function of AF CCD strip and FOV, obtained from the running solution. For each trend, the median value for the various contributing calibration units is plotted. This demonstrates the general stability of the calibration and the similar levels of goodness-of-fit achieved for the two FOVs, which for the PSF solutions use different sets of basis components (see Figure 4). The goodness-of-fit for the AF1 devices is slightly worse than AF2-9. There are a number of factors that contribute to this. First, the PSF observations in AF1 are binned on-chip in 1x2 pixels ALxAC, such that the samples used in the fit tend to have higher signal to noise than AF2-9 and departures from the model are more significant. Both the LSF and PSF calibrations will be affected to some extent by the higher electronic read noise in AF1 (8.5e^- versus 4.3e^-; see Hambly et al. (2018) table 1). Also, the offset non-uniformity part of the electronic bias cannot for technical reasons be completely removed in AF1 (see Hambly et al. 2018, section 3.3), which leaves uncorrected instrumental signatures in the obser-

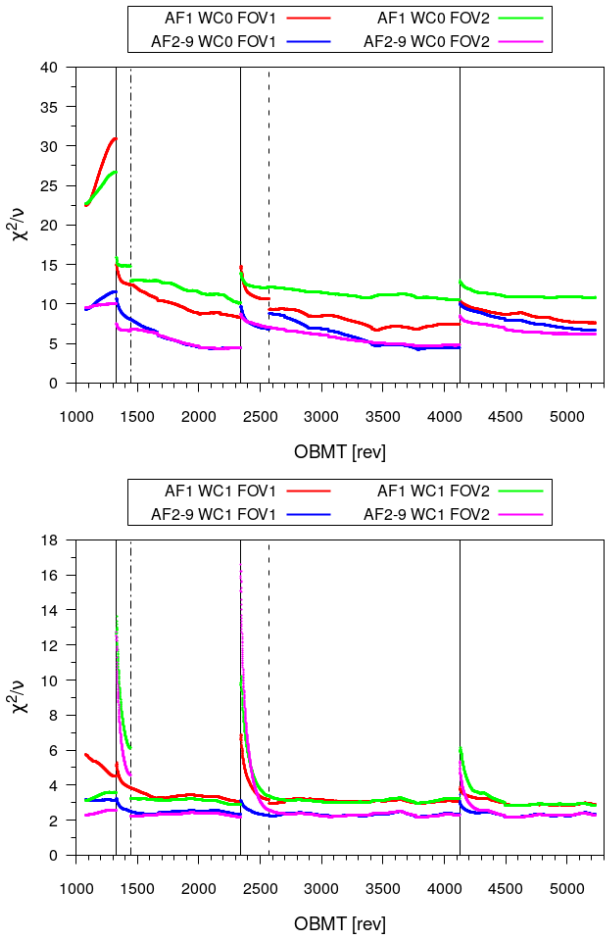

Fig. 14: Evolution of the median PLSF model goodness-of-fit statistic χ^2/ν over the EDR3 time range, as a function of AF CCD strip and FOV. The top panel corresponds to WC0 (PSF) calibrations and the bottom panel refers to WC1 (LSF) calibrations.

vations used in the PLSF fit. The χ^2/ν is also seen to be higher shortly after each decontamination; this is due to the issue described in section 5.1 where the rapid evolution of the PLSF as the instrument cools cannot be tracked accurately by the running solution.

Figure 15 shows an example of the median relative (top panel) and absolute (bottom panel) residuals about the model for a selection of observations used in the LSF calibration. The observations and corresponding model are from a single 1D calibration unit (FOV2, CCD row 1, strip AF5, gate 0, WC1) over 4020–4030 revolutions, although the results are representative of the whole focal plane. The observations span the corresponding magnitude range of $13 \lesssim G \lesssim 16$. These figures quantify the level of systematic errors present in the LSF calibration and the degree to which the model can reproduce the observations. There is clear structure present in the LSF core in the absolute residuals, suggesting the presence of unmodelled effects that are however rather modest in terms of their relative size. More significant in relative terms are the departures in the wings, where the model is systematically larger than the observations by up to a few percent. We initially thought that this might indicate systematic errors in the background estimation, but experiments suggest this is not the case. Instead, this is likely caused by the best-fit model being slightly too broad (thus underestimating the

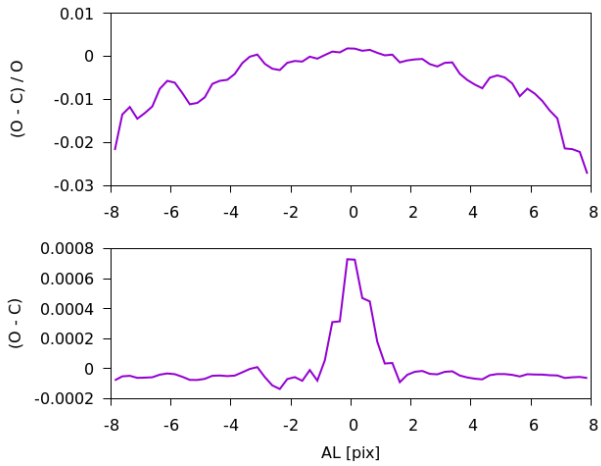

Fig. 15: Median relative (top) and absolute (bottom) residuals about the model for a selection of 1D observations used in the LSF calibration. Observations are selected from one calibration unit over a ten revolution period, and span the magnitude range $13 \lesssim G \lesssim 16$.

core flux and overestimating the wings), due ultimately to limitations associated with the set of basis components. This will be addressed in future data releases by updating the basis components (see section 6.7.4).

Figure 16 shows the analogous plots of the 2D residuals about the PSF model, for the WC0 calibration of the same device, gate, FOV, and time range. In this case the corresponding magnitude range is $12 \lesssim G \lesssim 13$. The residuals about the PSF model are much stronger and show significant structure in the core, with departures up to 20%. The residuals are also highly dependent on AC rate, with more significant departures up to 30–40% at times in the steep parts of the profile. The residuals have weaker dependence on AC rate for the shorter gates, indicating a problem with the PSF model regarding the AC rate dependence. This is discussed in detail in section 6.1.

Finally, in Figure 17 we show the distribution of normalised residuals about the model (solid green lines), for the LSF (left) and PSF (right) datasets presented in Figures 15 and 16. The unit Gaussian is plotted with a dashed purple line. These indicate that for neither dataset are the departures from the model consistent with the estimated errors on the observations, indicating that the model is incomplete and/or the errors on the observations are not correctly estimated. The inconsistency is much stronger for the PSF, and this is also reflected in the high value of the χ^2/ν statistic shown in Figure 14. While to some extent it is known that the model is not complete (e.g. it includes only linear effects), the large discrepancy between the LSF and PSF suggests a significant component of the PSF model may be missing. Again, this is dicussed in section 6.1.

5.5. Calibration uncertainties

In addition to the solution for the PLSF parameters the calibration pipeline computes the associated covariance matrix, by propagating the uncertainties on the observations through the partial and running solutions. This information can be used to compute the covariance matrix on the basis component amplitudes at a particular location in the observation parameter space, and finally to compute the covariance matrix on the PLSF samples. This provides an estimate of the calibration uncertainty and

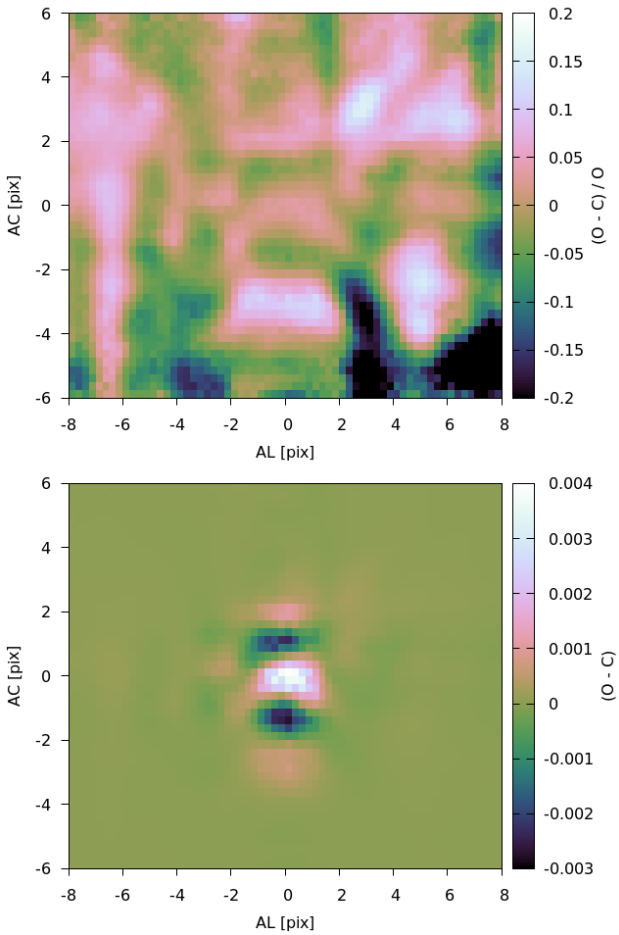

Fig. 16: Median relative (top) and absolute (bottom) residuals about the model for a selection of 2D observations used in the PSF calibration. Observations are selected from one calibration unit over a ten revolution period, and span the magnitude range $12 \lesssim G \lesssim 13$.

can reveal regions of the parameter space that are less well constrained.

A useful diagnostic is the square root of the trace of the covariance matrix on the PLSF samples—equivalent to the standard deviation of the sum of the samples. This quantifies the calibration uncertainty in a single number that is useful for investigating trends. For example, in Figure 18 we depict the evolution of this quantity over the whole EDR3 time range, for both the long gate PSF calibrations (top panel) and LSF calibrations (bottom panel), averaged over all AF2-9 devices and split by FOV. The calibration uncertainty shows signficant time-varying features. It is largest immediately before or after resets of the PLSF running solution; this is because at these times the running solution is less well constrained, having been produced from the merger of fewer partial solutions. In the periods between the solution resets there are significant peaks and troughs. The troughs coincide with Galactic plane scans, when the rate of observations is much higher and covers a wider range of $\nu_{\rm eff}$ leading to improved constraint on the model parameters. For the LSF model both FOVs achieve a similar level of constraint, however for the PSF model FOV2 is systematically less well constrained than FOV1. This is likely due to the fact that the PSF model uses different sets of basis components to model FOV1 and FOV2;

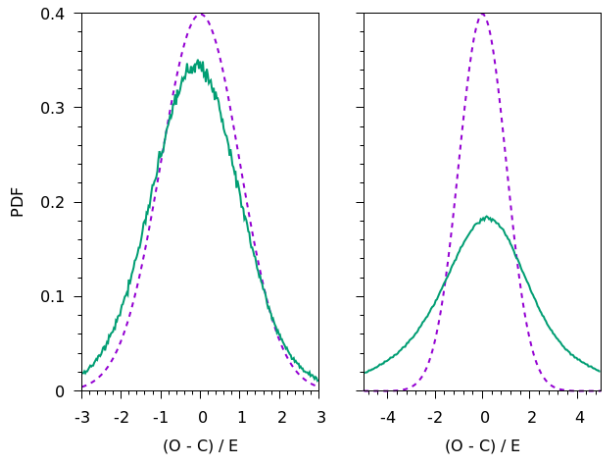

Fig. 17: Distribution of the normalised residuals about the model, for selected 1D LSF (left) and 2D PSF (right) calibrations. The data is plotted in solid green lines, and the dashed purple line shows the unit Gaussian.

the two sets are unlikely to offer the same level of accuracy in reproducing the observations.

Figure 19 depicts the AL variation in the calibration uncertainties for a single realisation of the LSF model. In the top panel the red line indicates the standard deviation of the LSF model shown in the bottom panel. The green points indicate the locations of the 18 samples that would be observed in a real *Gaia* window. There is some notable structure present here. First, the dip in the core is due to the way that location errors on the observations used in the LSF calibration are propagated to the errors on the sample values; this inflates the errors in the steep parts of the profile, such that the steep wings are less well constrained than the flatter core. Second, the increase in $\sigma_{\rm LSF}$ around AL ~ -8.5 arises because the observations used to calibrate this LSF (which corresponds to FOV1, CCD row 4, strip AF5) are systematically shifted from the window centre such that the LSF is this region is not well sampled by the data and the model is less well constrained. This is a general feature of the way that *Gaia* operates; the FOV2 observations in the same device are offset in the opposite direction and the corresponding LSF model is well constrained in this region (but not at AL ~ 8.5).

Finally, Figure 20 depicts the full covariance matrix for the model samples indicated by the green points in Figure 19. We note the presence of large off-diagonal terms, particularly in the LSF core (central part of the plot), that indicate the existence of significant covariances between the model samples. While for a given observation the noise on each sample is independent, the same is not true of the samples drawn from the calibrated PLSF model. This is a statistical property of the model that may need to be considered by downstream *Gaia* systems that make use of the PLSF calibration. Figure 21 provides a complementary plot of the correlation statistic, which gives a better impression of the relative importance of the covariance terms and distinguishes between negative and positive values. The most important feature is the presence of a negative correlation on the uncertainties between neighbouring samples.

6. Discussion

The PLSF modelling and calibration performed for *Gaia* EDR3 represents a major step forwards relative to DR1 and DR2, in

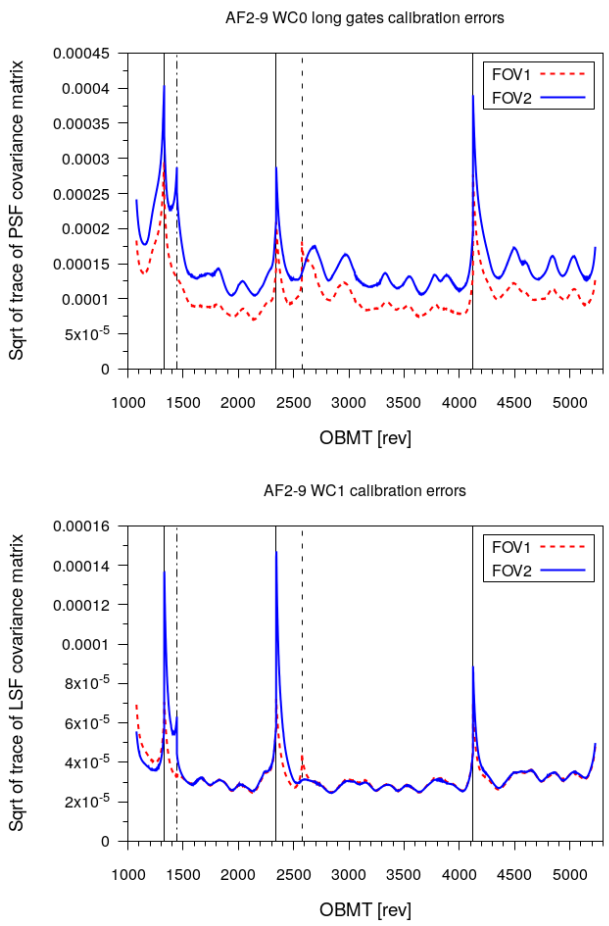

Fig. 18: Time evolution in the calibration uncertainty, quantified using the square root of the covariance matrix on the PLSF samples at a particular point in the observation parameter space. The vertical lines indicate resets of the PLSF running solution, as indicated in Table 6.

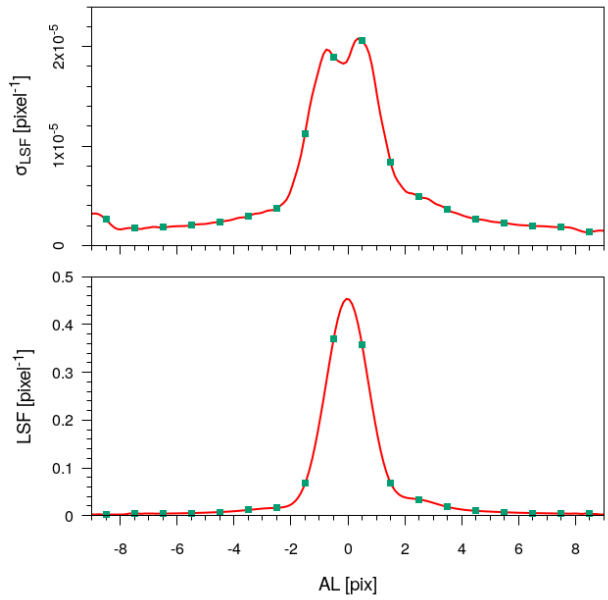

Fig. 19: AL variation in the calibration errors for a single representative realisation of the LSF model. The top panel depicts the standard deviation of the LSF model from propagation of the covariance on the LSF parameters; the lower panel depicts the corresponding LSF value. There is notable structure in the top panel, as explained in the text. The green points correspond to the locations of the samples for which the full covariance matrix is shown in Figure 20.

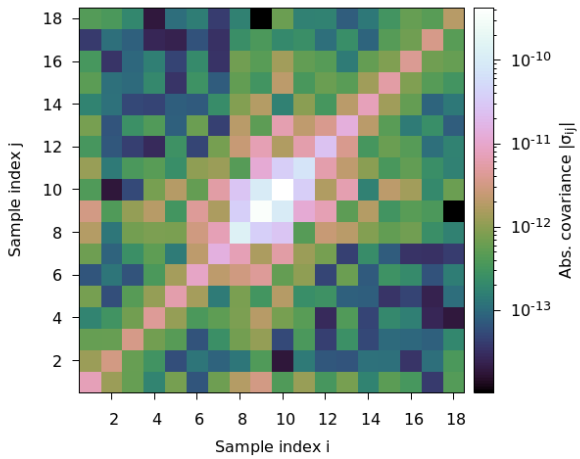

Fig. 20: Covariance matrix for the model LSF samples shown in Figure 19, in terms of the absolute value of the covariance for clarity of plotting. There are significant non-zero covariance terms between pairs of model samples, particularly in the core of the profile. This is in stark constrast to the observations used to calibrate the model, for which the errors on each sample are independent.

particular with the activation of the time and colour dependences, introduction of a full 2D PSF model, and the first closure of the iterative loop with the astrometric solution. However, the PLSF models as currently formulated are known to be incomplete, excluding, for example, magnitude dependent effects, and being subject to various compromises and approximations that are the consequence of unavoidable limitations in the data processing chain. Extensive analysis of the calibration results carried out since the pipeline was executed has clarified the directions for future development, and also revealed some defects with the current modelling, alluded to earlier in this paper, that will be corrected in later data releases. In this section we discuss some of these issues.

6.1. Missing AL rate dependence in PSF model

Undoutedly the most significant problem with the current PLSF modelling is the presence of a systematic error in the PSF model, particularly for long gates (gate 11, 12 and 0), that has a strong correlation with AC rate. This manifests as a bimodality in the calibrated PSF that is evident in Figure 13 and also reflected in the spatial structure in the residuals (Figure 16) and in their distribution (Figure 17, right panel). This issue has undergone extensive investigation since the calibration was performed, and is now understood to be caused largely by the presence of an additional PLSF dependence that is absent from the model, that of the along-scan rate.

In the TDI mode in which *Gaia* operates, the (fixed) rate of parallel charge transfer must be closely matched to the rate at which stellar images drift across the CCDs, which in turn is determined by a combination of the scan rate and the AL an-

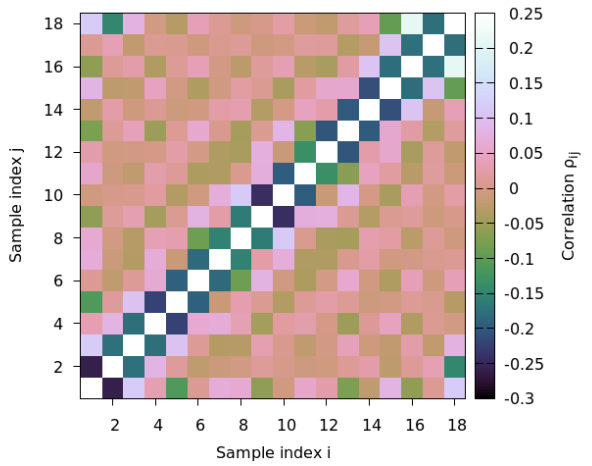

Fig. 21: Correlation statistic $\rho_{ij} = \sigma_{ij}/(\sigma_i\sigma_j)$ for the model LSF sample uncertainties shown in Figure 19. The diagonal elements all have $\rho_{ij} = 1$ and have been eliminated in order to avoid stretching the colour scale. The main feature is a negative correlation on the uncertainties between neighbouring samples.

gular pixel scale. Any mismatch between the two has the effect of broadening the apparent PSF in the AL direction, as the stellar image gradually lags behind or moves ahead of the integrating charge during exposure. The AL scan rate is continuously adjusted to match the TDI rate as closely as possible, and it is subject to both systematic and random variations induced by the *Gaia* scan law (see Gaia Collaboration et al. 2016, section 5.2) and various disturbances such as micro-meteorites and thermo-mechanical 'clanks'. The component induced purely by the scan law varies sinusoidally with a period of one revolution and an amplitude of up to ~0.03 pixels per second. It is caused by a rotation of the field arising from the precessional motion and not, for example, by a variation in the satellite rotation rate. The same effect gives rise to the AC rate modulation, which is much larger. The scan-law component of the AL rate varies in strength and sign across the focal plane, is out of phase by $\pi/2$ with the associated AC rate modulation in the same telescope and is out of phase between the two telescopes by 106.5°. The AL angular pixel scale also differs systematically between the two telescopes due to focal length differences, and varies across the focal plane depending on the distance from the optical axis. The result is that the AL image rate differs significantly from the parallel charge transfer rate, which violates the assumptions of both the LSF and PSF model and leads to some importance consequences.

The observable effect on the LSF is relatively minor, and leads to a slight broadening of the profile by up to ~0.1 pixels that varies over a revolution; the time dependence in the LSF solution lacks the resolution to capture this so that in effect the LSF solution fits the average profile, and the effects on the astrometry and photometry are minimal. However, the effect on the PSF is stark. The combination of the out-of-phase AL and AC rates induces a shear on the PSF that varies in sign and magnitude over the course of one revolution. This is depicted in Figure 22, which compares the observed FOV1 PSF (from aligned and stacked observations) at maximum negative (left panel) and positive (middle panel) values of the AC rate, half a revolution apart. At the AC rate extrema the AL rate variation is minimal (due to the $\pi/2$ phase difference), so that only the zeropoint offset remains and the AL rate takes on a single value. In such a situation the existing PSF model is in principle able to reproduce the observations via the AC rate dependence, and it is interesting to note that the difference between the two plots (shown in the third panel) closely matches one of the low-order FOV1 basis components shown in Figure 4, indicating that the model is attempting to fit the average shearing. However, in general the relation between the AL and AC rate is not monotonic, and no model that considers only the AC rate can accurately reproduce the PSF. This effect is much stronger for longer integration times as this leads to larger total AL and AC displacements. In terms of the CCD gates, the effect is strongest for gate 0 and negligible for gate 10, so the impact on the astrometry and photometry is expected to be largest for sources in the corresponding magnitude range of $11.5 \lesssim G \lesssim 13$.

The combined effects of AL and AC rate could be naively incorporated into the PSF model by adding the AL rate as another dimension in the observation parameter space. However, this approach faces numerous problems due to the curse of dimensionality: The sparsity of the observations within the parameter space makes the model difficult to constrain, and the explosion in the number of PSF parameters (and covariances) makes the calibration too computationally demanding. Fortunately, the effects of the AL and AC rate can be modelled quite successfully from first principles as a convolution with a top hat kernel of the appropriate width and orientation. This avoids the need to calibrate the effects empirically and thus eliminates the associated PSF parameters. An analytical model that performs this has been developed and integrated into the PLSF pipeline for use in future *Gaia* data releases. This will be described in more detail in a dedicated publication.

6.2. Uncertainty estimation for PSF observations

The systematic error in the calibrated PSF model was also found to be partly due to inappropriate weighting of the samples used to constrain the model. As described in section 4.1.3, the estimated error on each sample includes a contribution to account for uncertainty on the predicted location of the source. This increases the error in steeper parts of the profile where the effects of location errors are more significant. The motivation is to down-weight observations with larger location uncertainty, which include a greater fraction of outliers such as undetected close pairs. However, this also has the undesirable effect of reducing the constraint in the steep parts of the profile for all sources, and results in a solution that preferentially fits the flatter regions of the profile that do not carry as much astrometric constraint (although these regions are more useful to the photometry). This can be seen clearly in Figure 19. The effect is much greater on the PSF calibration than the LSF because for the PSF the uncertainty on the AC location is also included, and in the 2D observations there are relatively fewer samples in the steep parts of the profile than for the 1D observations so they are further down-weighted. For future *Gaia* data releases this procedure will be avoided, and outlying observations will be handled by other methods.

6.3. Incomplete colour calibration for PSF

Both the astrometric and photometric processing encountered issues that suggest the colour calibration of the PSF was less successful than for the LSF. In the astrometric processing, this manifested as a strong residual chromaticity for the 2D observations compared with 1D (see Lindegren, Lennart et al. 2020, appendix A.4). In the photometric processing, a colour term was present in the G band for $G < 13$ (corresponding to 2D observations) but

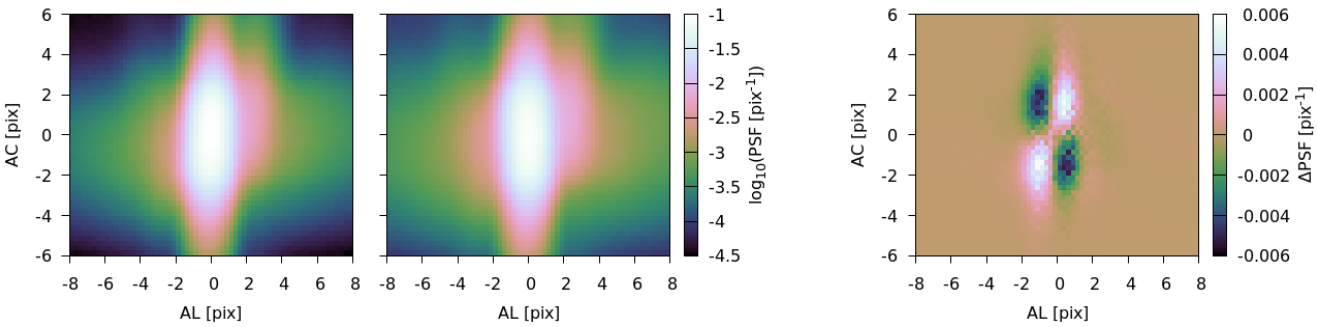

Fig. 22: Effects of AC and AL rate variations on the observed PSF. The two panels on the left depict many stacked observations from FOV1 ROW1 AF6 gate 0, for two narrow ranges of AC rate at high negative (-1.0 → -0.95 pix/s; left) and high positive (0.95 → 1.0 pix/s; middle) values. These reveal an apparent shear between the two PSFs that is clear in a plot of the difference (right panel). This effect is induced by non-zero AL rate, as explained in the text.

not for fainter, 1D observations (see Riello et al. 2020, section 7). The reason for this is most likely due to differences in the basis components used by the LSF and PSF models and the major dependences that are active. The LSF model used 25 1D basis components that are tuned to empirically model only the colour dependence, whereas the PSF model used 30 basis components that are tuned to model both the colour and AC rate dependences. The AC rate dependence has a very large effect on the profile, which for a fixed number of basis components in effect reduces the ability to model colour variations. This issue will hopefully be solved in later data releases by the analytic modelling of the AC rate (and AL rate) dependence in the PSF, which means that the 2D basis components can be tuned for empirical modelling of the colour dependence only.

6.4. Use of a reference PLSF calibration

A fixed reference PLSF calibration is used at several points in the calibration pipeline—see section 4.1.3. The reference calibration was solved in a separate procedure by fitting the PLSF model to observations selected from a stable period of low contamination, using an iterative solution to reject outliers and update the normalisation of each observation. This produces a clean calibration that is suitable for use in the main pipeline for outlier detection, computing corrections to the observation errors, and in normalising the observations to account for flux falling outside the window area. The last of these applications contains some subtleties that require further discussion.

The LSF and PSF models are normalised to unity, over the whole AL dimension for the LSF and over the AL and AC dimensions for the PSF. Due to the finite extent of the windows, each observation sees only a fraction of the total flux received from a source—the enclosed energy fraction. The observations that are used to calibrate the LSF and PSF models must be normalised to match the requirements of the model, and if the enclosed energy fraction is not accurately accounted for then the model can end up trying to force flux into or out of the unobserved regions beyond the window boundary in order to better fit the observed samples, which invariably introduces artefacts in the shape.

One way to estimate the enclosed energy fraction for a particular observation of a known G band magnitude source is to invert the photometric calibration and compute the associated instrumental flux. This provides an estimate of the total number of photoelectrons in the detector, and the ratio between the observed number of photoelectrons within the window and the total number gives the enclosed energy fraction. We note that for the LSF the fraction of flux lying outside of the window in the AC direction (the 'AC flux loss') must also be accounted for—this is included as part of the photometric calibration (Riello et al. 2020). This is conceptually similar to the closure of the iterative loop with the astrometric calibration, where the use of predicted locations to calibrate the PLSF enables a greater consistency and separation of effects between the two systems–though care must be taken to avoid circularity and feedback of systematic errors.

However, this method cannot be used, owing mainly to the fact that the PLSF calibration pipeline runs before the photometric calibration in the *Gaia* processing chain. A workaround that has been adopted for EDR3 is to use the fixed reference PLSF calibration to estimate a physically reasonable value for the enclosed energy fraction of each observation, from the sum of the model samples within the window area. This value is accurate to around the ~1% level, which is sufficient to allow the PLSF models to converge to a solution that accurately reproduces the PLSF shape. This leaves systematic errors in the PLSF normalisation of around ~1%, which propagate to the estimated fluxes of observations derived from PLSF fitting, and are then corrected as part of the photometric calibration. So this method has limited impact on both the astrometry and photometry and provides a suitable solution for EDR3.

However, certain improvements in the CCD reductions and instrument modelling that are under development for future data releases cannot tolerate systematic errors in the PLSF calibration at this level. These include, for example, the modelling of non-linear magnitude-dependent effects that are highly sensitive to the number of photoelectrons in each pixel. Therefore, future developments to the PLSF calibration will aim to reduce these systematic errors further. This may be done by introducing limited calibrations of the system throughput earlier in the pipeline, in order to perform a rudimentary inversion of the photometric calibration that will allow these effects to be properly calibrated in the PLSF and not enforced *a priori*.

6.5. Tracking of rapidly evolving instrument state

The running solution that is used to calibrate the time dependence of the PLSF parameters (see sections 3.4.5 and 4.3) successfully tracks the gradually evolving instrument state during nominal periods. However, shortly after a decontamination there is a period of thermal instability during which the instrument state evolves rapidly and the running solution fails to converge on the instantaneous solution (see Figure 10). This situation can

be improved either by reducing the time decay constant in the running solution, to allow faster convergence at the expense of reduced smoothing of noise, or by excluding a greater segment of the data during the period of thermal instability. This will be investigated for future *Gaia* data releases.

6.6. Use of a single colour parameter

The effective wavenumber $\nu_{\rm eff}$ is a good parameterisation of the source colour as the chromatic shifts for sources with normal stellar SEDs are expected to be linear in $\nu_{\rm eff}$ (de Bruijne et al. 2006). It is also convenient from the calibration point of view, as it is a single number and its value is restricted to a relatively narrow range. However, it does introduce limitations when processing sources that have non-stellar SEDs, such as quasars or emission line objects. Other extended parameterisations of the source colour, such as the spectral shape coefficients (see Riello et al. 2020, section 4.4) may offer better colour parameterisations for these sources. However, this complicates the calibration as such objects are rare, and a degradation of the modelling in these cases may have to be accepted.

6.7. Improvements for DR4 and beyond

In addition to dealing with the various problems described earlier in this section, there are a range of improvements to the PLSF models that are planned for future data releases. A brief description of these is presented in this section. At the time of writing, some have already been implemented for DR4 and are in the final stages of testing. These will be described in detail in a dedicated publication, but in anticipation of these advances they are summarised here.

6.7.1. Analytic modelling of AL and AC rate effects

The effects of AL and AC rate present significant problems to the EDR3 PSF modelling in particular, and cannot be calibrated empirically (see section 6.1). However, unlike the other dependences the effects of AL and AC rate on the PLSF can be derived from first principles, and modelled accurately as a convolution with a top hat of an appropriate width and orientation. This will be implemented in future PLSF modelling and will lead to improved PLSF reconstruction with reduced number of parameters.

6.7.2. Calibration of AL and AC shift parameters

The LSF model presented in Equation 1 includes a parameter u_0 that corresponds to a pure shift of the LSF profile in the AL direction without a change in shape. The PSF model has an additional parameter corresponding to shifts in the AC direction. The LSF model is non-linear in u_0 which makes the calibration of it significantly more challenging, and in EDR3 this parameter is not calibrated and instead is fixed at zero. This has the effect of allowing any shifts in the profile to be absorbed into the calibration of the other parameters and modelled by appropriate weighting of the H_n basis components.

The PLSF model is calibrated to the predicted locations of sources provided by the source astrometry combined with the attitude and geometric instrument calibrations. In principle a perturbation in the geometric calibration leads to a displacement of the predicted locations of sources that is compensated for by a similar shift in the PLSF calibration. There is thus a degeneracy between the geometric instrument calibration and the PLSF origin. The key to breaking this degeneracy is to make an accurate calibration of the u_0 parameter, including its variation with time, source colour, and other parameters. This can then be used to enforce constraints on the PLSF model that allow a full separation of the PLSF and geometric calibrations. This will be implemented for future data releases.

6.7.3. Inclusion of magnitude-dependent effects

The PLSF model includes only the linear component of the CCD response arising purely from optical effects. However, there are numerous second-order components of the CCD response that are non-linear in the source flux, and that have complex dependences on both the flux and other parameters, resulting in redistribution and/or loss of charge entirely from the window. These effects are introduced by several phenomena that manifest in the *Gaia* CCDs, including deflection of incoming photoelectrons by large charge packets (the 'brighter-fatter' effect, Antilogus et al. (2014)), blooming (in conjunction with strong spatial variations in the performance of the anti-blooming drains), and AL variation in the pixel well capacity (which in conjunction with the TDI mode of operation introduces non-linearity to the CCD response at high signal levels). The CCDs are also affected by CTI in the image section, which redistributes charge in the AL direction, and CTI in the serial register, which redistributes charge in the AC direction. CTI in particular is an important component that has complex dependences on the source magnitude, CCD illumination history and, for serial CTI, the readout sequence, which varies from one TDI line to the next and is determined by the distribution of windows along the serial register. The existence of a supplementary buried channel in the CCD image section is expected to introduce a break in CTI behaviour for faint stars. Extensive work was done pre-launch on quantifying the effects of CTI on observations of stars (e.g. Prod'homme et al. 2011), and continued investigation using in-flight data will benefit greatly from an accurate calibration of the linear part of the PLSF.

In terms of modelling all of these effects, it is clear that simply extending the PLSF parameterisation to include source flux is not sufficient. Instead, it is anticipated that the PLSF model will continue to include only the linear part of the CCD response, and the various non-linear components will be incorporated via a separate forward-model of the CCD pixel-level behaviour. In this scenario, the existing PLSF model will predict the spatial distribution of incoming photons, which in turn provides the inputs for the next stage of modelling the CCD response.

6.7.4. Improvements to the basis components

The 1D basis components used to model the LSF (and, indirectly, the PSF) for EDR3 were produced pre-launch using simulations of the optical system, as described in section 3.2 and in detail in Lindegren (2009) (see also Figures 2 and 4). While these have been sufficient for EDR3, for future data releases we are investigating whether updates to the basis components may offer significant improvements to the PLSF reconstruction. Recent analysis has revealed some minor numerical artefacts in the optical model discretisation and the interpolation of the individual bases, as explained in Montegriffo (2017). The bases are also not fully orthogonal, and are computed in the AL direction only. More significant is the possibility that the optical model fails to include some important elements of the instrument. This can result in basis components that fail to reproduce certain variations

present in the data, leading to systematic errors. For example, it is now known that the wavefront error includes a significant systematic component arising from mirror polishing artefacts in the primary mirrors, and this is absent from the original optical model. We therefore intend to revise the simulation code to fix these various issues, and to investigate the limitations of the basis components to identify any elements missing from the optical model.

6.7.5. Independent calibration of SM

The calibration of the PSF for the SM instrument faces numerous challenges, as described in section 5.3, and for EDR3 an independent calibration of SM was not possible. While in EDR3 this has limited impact, data products planned for future releases may wish to make greater use of the SM observations and will require an accurate calibration of the PSF. For example, SM observations are not currently used in either the astrometric or photometric solutions for each source. Also, certain selected dense regions of the sky are scanned using a special mode where, in addition to the normal source detection and windowing, the full SM images are downlinked without windowing. These data are presently not used, and any future processing of them will require a dedicated calibration of the SM PSF. Future developments of the PSF model and pipeline will aim to overcome the challenges presented by SM so that an independent calibration can be achieved.

6.7.6. Bootstrapping of attitude and geometric calibration

One of the challenges faced in the production of the PLSF calibration for EDR3 was the need to obtain predicted locations for sources during the first iteration of the solution, which occurred before AGIS had computed the required attitude and geometric calibrations. This had to be overcome by using the calibrations from DR2 as the starting point, supplemented with calibrations taken from the *Gaia* realtime pipeline to cover the additional time segment after the end of DR2 and before the end of EDR3. This introduced an inhomogeneity in the data that resulted in some systematic errors in the first iteration of the PLSF calibration that required an additional iteration with AGIS to reduce.

This reliance on inputs from previous cycles and other sources, computed using different generations of the instrument models, to initialise the PLSF calibration risks introducing artefacts and systematic errors that may be hard to eradicate. For future data releases, a new bootstrapping of the attitude and geometric calibrations is being developed that will provide a homogeneous and consistent set of inputs for initialising the PLSF calibration.

6.7.7. Far PSF calibration

The PLSF models implemented for EDR3 cover only the core of the profile contained within the *Gaia* windows for nominal observations. There are several applications within the *Gaia* data processing systems that require a calibration of the PSF over a much wider range. These include the analysis of very bright stars for which the entire core region is saturated, and the background modelling for normal stars in the vicinity of bright stars. For various reasons the PSF model presented in this paper cannot be easily adapted to model the extended profile of bright stars. For future data processing cycles a new model is under development that aims to provide a suitable calibration of the extended PSF.

7. Conclusions

The PLSF modelling and calibration carried out for *Gaia* EDR3 represents a major step forwards in the data processing, and will contribute to reduced systematic errors in the core mission data products. This is reflected in both the astrometric and photometric solutions for EDR3, which see improvements relative to DR2 beyond those expected from the increased number of observations alone (see e.g. section 5.4 and appendix A.1 in Lindegren, Lennart et al. (2020), and section 9.5 in Riello et al. (2020)).

In this paper we have presented a detailed description of the models, the pipeline and the calibration products that is necessary for a complete understanding of the EDR3 contents and survey properties. These developments are part of an ongoing process of gradual refinement and improvement as the instrument modelling increases in fidelity and we gain a deeper understanding of the data. Further significant improvements are expected in the future data releases.

Acknowledgements. The authors would like to thank the referee Jay Anderson for insightful comments that have improved the quality and clarity of this paper. This work has made use of data from the European Space Agency (ESA) mission *Gaia* (`https://www.cosmos.esa.int/gaia`), processed by the *Gaia* Data Processing and Analysis Consortium (DPAC, `https://www.cosmos.esa.int/web/gaia/dpac/consortium`). Funding for the DPAC has been provided by national institutions, in particular the institutions participating in the *Gaia* Multilateral Agreement. The *Gaia* mission website is: `http://www.cosmos.esa.int/gaia`. The work described in this paper has been financially supported by the United Kingdom Particle Physics and Astronomy Research Council (PPARC), the United Kingdom Science and Technology Facilities Council (STFC), and the United Kingdom Space Agency (UKSA) through the following grants to the University of Bristol, the University of Cambridge, the University of Edinburgh, the University of Leicester, the Mullard Space Sciences Laboratory of University College London, and the United Kingdom Rutherford Appleton Laboratory (RAL): PP/D006511/1, PP/D006546/1, PP/D006570/1, ST/I000852/1, ST/J005045/1, ST/K00056X/1, ST/K000209/1, ST/K000756/1, ST/L006561/1, ST/N000595/1, ST/N000641/1, ST/N000978/1, ST/N001117/1, ST/S000089/1, ST/S000976/1, ST/S001123/1, ST/S001948/1, ST/S002103/1, and ST/V000969/1; the Spanish Ministry of Economy (MINECO/FEDER, UE) through grants ESP2016-80079-C2-1-R, RTI2018-095076-B-C21 and the Institute of Cosmos Sciences University of Barcelona (ICCUB, Unidad de Excelencia 'María de Maeztu') through grants MDM-2014-0369 and CEX2019-000918-M; the German Aerospace Agency (Deutsches Zentrum für Luft- und Raumfahrt e.V., DLR) through grants 50QG0501, 50QG0601, 50QG0602, 50QG0701, 50QG0901, 50QG1001, 50QG1101, 50QG1401, 50QG1402, 50QG1403, and 50QG1404 and the Centre for Information Services and High Performance Computing (ZIH) at the Technische Universität (TU) Dresden for generous allocations of computer time; the Agenzia Spaziale Italiana (ASI) through contracts I/037/08/0, I/058/10/0, 2014-025-R.0, 2014-025-R.1.2015 and 2018-24-HH.0 to the Italian Istituto Nazionale di Astrofisica; and the Swedish National Space Board (SNSB/Rymdstyrelsen). AB additionally acknowledges financial support from the Netherlands Research School for Astronomy (NOVA). Finally, the authors also acknowledge the computer resources from MareNostrum, and the technical expertise and assistance provided by the Red Española de Supercomputación at the Barcelona Supercomputing Center, Centro Nacional de Supercomputación.

References

Anderson J., King I.R., Oct 2000, PASP, 112, 1360
Antilogus P., Astier P., Doherty P., Guyonnet A., Regnault N., Feb. 2014, Journal of Instrumentation, 9
Bertin E., Jul. 2011, In: Evans I.N., Accomazzi A., Mink D.J., Rots A.H. (eds.) Astronomical Data Analysis Software and Systems XX, vol. 442 of Astronomical Society of the Pacific Conference Series, 435
Bierman G.J., 1977, Factorization Methods for Discrete Sequential Estimation, Dover
Boubert D., Everall A., Holl B., Jul. 2020, MNRAS, 497, 1826
Busonero D., Gai M., Gardiol D., Lattanzi M.G., Loreggia D., Apr. 2006, A&A, 449, 827
Busonero D., Lattanzi M.G., Gai M., Licata E., Messineo R., Aug. 2014, In: Modeling, Systems Engineering, and Project Management for Astronomy VI, vol. 9150 of Society of Photo-Optical Instrumentation Engineers (SPIE) Conference Series

Crowley C., Kohley R., Hambly N.C., et al., Nov. 2016, A&A, 595, A6
de Bruijne J.H.J., Lindegren L., Svensson O., et al., August 2006, Chromaticity in Gaia-3, URL http://www.rssd.esa.int/doc_fetch.php?id=2694426, GAIA-CA-TN-ESA-JDB-028
Fabricius C., Bastian U., Portell J., et al., 2016, A&A, 595, A3, URL https://doi.org/10.1051/0004-6361/201628643
Gaia Collaboration, Dec. 2020, Gaia EDR3 online documentation, URL https://gea.esac.esa.int/archive/documentation/GEDR3/index.html
Gaia Collaboration, Prusti T., de Bruijne J.H.J., et al., Nov. 2016, A&A, 595, A1
Gaia Collaboration, Brown, Anthony G.A., Vallenari, A., Prusti, T., de Bruijne, J. H.J., 2020, A&A, URL https://doi.org/10.1051/0004-6361/202039657
Green D.A., Jun. 2011, Bulletin of the Astronomical Society of India, 39, 289
Hambly N.C., Cropper M., Boudreault S., et al., 2018, A&A, 616, A15, URL https://doi.org/10.1051/0004-6361/201832716
Hobbs D., Clotet M., Castañeda J., et al., Jul. 2018, Gaia DR2 documentation Chapter 2: Astrometric and photometric pre-processing, Gaia DR2 documentation
Lindegren L., May 2003, Representation of LSF and PSF for GDAAS-2, URL http://www.rssd.esa.int/doc_fetch.php?id=357835, GAIA-LL-046
Lindegren L., November 2008, A general Maximum-Likelihood algorithm for model fitting to CCD sample data, URL http://www.rssd.esa.int/doc_fetch.php?id=2861864, gAIA-C3-TN-LU-LL-078
Lindegren L., August 2009, Minimum-dimension LSF modelling, URL http://www.rssd.esa.int/doc_fetch.php?id=2915742, GAIA-C3-TN-LU-LL-084
Lindegren L., September 2010a, LSF modelling with zero to many parameters, URL http://www.rssd.esa.int/doc_fetch.php?id=, GAIA-C3-TN-LU-LL-088-02
Lindegren L., November 2010b, A generic LSF/PSF model and its role in IDT, FL, IDU and AGIS, URL http://www.rssd.esa.int/doc_fetch.php?id=3049410, GAIA-C3-TN-LU-LL-089
Lindegren L., October 2010c, A posteriori reduction of the set of basis functions for LSF modelling, URL http://www.rssd.esa.int/doc_fetch.php?id=, GAIA-C3-TN-LU-LL-090-01
Lindegren L., Hernández J., Bombrun A., et al., 2018, A&A, 616, A2, URL https://doi.org/10.1051/0004-6361/201832727
Lindegren, Lennart, Klioner, S. A., Hernández, J., et al., 2020, A&A, URL https://doi.org/10.1051/0004-6361/202039709
Montegriffo P., September 2017, XP LSF modelling, GAIA-C5-TN-OABO-PMN-012-1 PENDING ADDITION TO THE GAIA PUBLIC DOCUMENTS PAGE
Prod'homme T., Brown A.G.A., Lindegren L., Short A.D.T., Brown S.W., Jul. 2011, MNRAS, 414, 2215
Refregier A., Jan 2003, MNRAS, 338, 35
Riello M., De Angeli F., Evans D.W., et al., 2020, A&A, URL https://doi.org/10.1051/0004-6361/202039587
Stetson P.B., Mar. 1987, PASP, 99, 191
Torra, Ferran, Castañeda, J., Fabricius, C., et al., 2020, A&A, URL https://doi.org/10.1051/0004-6361/202039637
van Leeuwen F. (ed.), 2007, Hipparcos, the New Reduction of the Raw Data, vol. 350 of Astrophysics and Space Science Library